

# Continuum Modeling of Micro-particle Electrorotation in Couette and Poiseuille Flows—the Zero Spin Viscosity Limit

Hsin-Fu Huang <sup>a, b</sup>, Markus Zahn <sup>\*, b</sup>, Elisabeth Lemaire <sup>c</sup>

<sup>a</sup> *Department of Mechanical Engineering, Massachusetts Institute of Technology, Cambridge, MA 02139, USA*

<sup>b</sup> *Laboratory for Electromagnetic and Electronic Systems, Research Laboratory of Electronics, Department of Electrical Engineering and Computer Science, Massachusetts Institute of Technology, Cambridge, MA 02139, USA*

<sup>c</sup> *Laboratoire de Physique de la Matière Condensée, CNRS-Université de Nice-Sophia Antipolis, 06108 Nice cedex 2, France*

## Abstract

A continuum mechanical model is presented to analyze the negative electrorheological responses of a particle-liquid mixture with the suspended micro-particles undergoing Quincke rotation for both Couette and Poiseuille flow geometries by combining particle electromechanics and continuum anti-symmetric/couple stress analyses in the zero spin viscosity limit. We propose a phenomenological polarization relaxation model to incorporate both the micro-particle rotation speed and macro-continuum spin velocity effects on the fluid polarization during non-equilibrium motion. Theoretical predictions of the Couette effective viscosity and Poiseuille flow rate obtained from the present continuum treatment are in good agreement with the experimental measurements reported in current literature.

*Keywords:* Electrohydrodynamics; Electrorotation; Quincke rotation; Negative electrorheological effect; Continuum anti-symmetric/couple stress tensor

\*Corresponding author: TEL: +1-617-253-4688; FAX: +1-617-258-6774; *E-mail address:* [zahn@mit.edu](mailto:zahn@mit.edu) (Prof. M. Zahn)

## 1. Introduction

Electrorheological (ER) fluids are a class of fluids that consist of conducting or insulating dielectric solid micro-particles suspended within a dielectric liquid medium. Due to the electrical property (*e.g.*, conductivity and/or permittivity) mismatch between the solid and liquid phases, one can control the apparent macroscopic properties of the ER fluid such as the effective viscosity for suspensions via the application of external direct current (DC) or alternating current (AC) electric fields. Literature has therefore categorized ER effects, based on the flow or rheological responses, into either positive ER or negative ER phenomena when the fluid suspension is subjected to electric fields [1-6].

Upon the application of DC electric fields, Foulc *et al.* [4] discussed the important role of electrical conductivities of the respective solid and liquid phases in determining the inter-particle electrical force interactions in ER fluids. Boissy *et al.* [5] then further characterized and made distinctions of macroscopic positive and negative ER responses based on different relative magnitudes of the respective conductivities of the two phases. For ER fluids consisting of micro-particles with a conductivity,  $\sigma_2$ , larger than that,  $\sigma_1$ , of the carrier liquid, stable particle chains are formed in the direction of the electric field so that the macroscopic fluid resistance against externally applied shear perpendicular to the electric field is enhanced and result in an increased measured effective viscosity—the positive ER effect [1-3]. On the other hand, when the conductivity of the carrier liquid is larger than that of the micro-particles, *i.e.*,  $\sigma_1 > \sigma_2$ , laminated layers (perpendicular to the electric field) of packed particles resulting from electromigration are formed adjacent to one of the two electrodes leaving a portion of the ER fluid relatively clear of particles and hence leading to a reduction in the resistance against externally applied shear forces perpendicular to the electric field; a decrease in the effective viscosity is measured—the negative ER effect [5, 6].

Despite the relatively sparse reports on negative ER effects, recent experimental observations found that: (i) with a given constant shear rate or equivalently the Couette boundary driving velocity, the measured shear stress required to drive the Couette ER fluid flow is reduced (an effectively decreased viscosity) and (ii) at a given constant pressure gradient, the Poiseuille flow rate of the ER fluid can be increased both by applying a uniform DC electric field perpendicular to the direction of the flows [7-12]. The mechanism responsible for the apparent increased flow rate and decreased effective viscosity was attributed to the spontaneous electrorotation of the

1  
2  
3  
4 dielectric micro-particles suspended within the carrier liquid, which is a mechanism different  
5 from the traditional electromigration or particle electrophoresis explanation as mentioned in  
6 previous negative ER literature [5, 6]. This spontaneous particle rotation under the action of a  
7 DC electric field is often called “Quincke rotation” for G. Quincke’s systematic study done in  
8 1896 [13-18].  
9

10  
11  
12  
13 The origin of Quincke rotation can be illustrated by considering a dilute collection of  
14 insulating dielectric spherical particles with permittivity  $\varepsilon_2$  and conductivity  $\sigma_2$  suspended in a  
15 slightly conducting carrier liquid having a permittivity of  $\varepsilon_1$  and a conductivity of  $\sigma_1$ . The  
16 material combination is chosen so that  $\tau_2 > \tau_1$  where  $\tau_1 = \varepsilon_1/\sigma_1$  and  $\tau_2 = \varepsilon_2/\sigma_2$  are the charge  
17 relaxation time constants of the liquid and the particles, respectively. When a uniform DC  
18 electric field is applied across the dilute suspension, charge relaxation follows the Maxwell-  
19 Wagner polarization at the solid-liquid interfaces, and each of the suspended particles attains a  
20 final equilibrium dipole moment in the opposite direction to that of the applied DC field for the  
21 condition of  $\tau_2 > \tau_1$ . This, however, is an unstable equilibrium, and as the applied electric field  
22 reaches a critical value [17, 18], namely,  
23  
24  
25  
26  
27  
28  
29  
30  
31  
32

$$E_c \equiv \left(1 + \frac{\sigma_2}{2\sigma_1}\right) \sqrt{\frac{8\eta_0\sigma_1}{3\varepsilon_1\sigma_2(\tau_2 - \tau_1)}}, \quad (1)$$

33  
34  
35  
36 where  $\eta_0$  is the viscosity of the carrier liquid, the liquid viscous damping can no longer  
37 withstand any small perturbations misaligning the particle dipole moment and the applied DC  
38 field. The electrical torque resulting from the misalignment exceeds the viscous torque exerted  
39 on the micro-particle giving rise to spontaneous, self-sustained particle rotation either clockwise  
40 or counter clockwise with the rotation axis perpendicular to the planes defined by the electric  
41 field. When the particle-liquid suspension, or ER fluid, is driven by a boundary shear stress  
42 (Couette flow) or a pressure gradient (Poiseuille flow), the macroscopic flow vorticity gives the  
43 suspended micro-particles, instead of by random chance, preferable directions for rotation via  
44 viscous interactions once the external electric field (generally larger than the critical field,  $E_c$ ) is  
45 applied. It is this combined effect of microscopic electrorotation and macroscopic flow vorticity  
46 that gives rise to the newly observed negative ER phenomenon as described above [7-12].  
47  
48  
49  
50  
51  
52  
53  
54  
55  
56

57 Although models are given in current literature for analyzing the new phenomenon, they are  
58 focused on the dynamics of a single particle and the utilization of a two-phase volume averaged,  
59  
60  
61  
62  
63  
64  
65

1  
2  
3  
4 effective medium description [7-12, 19]. Little has been done in developing a continuum  
5  
6 mechanical model from a more classical field theory based starting point in predicting the  
7  
8 dynamical behavior of fluids consisting of micro-particles undergoing spontaneous  
9  
10 electrorotation. To the best of the authors' knowledge, the ferrofluid spin-up flow is the most  
11  
12 representative flow phenomenon arising from internal particle rotation in current rheology  
13  
14 research [20-27].

15  
16 In a ferrofluid spin-up flow, magnetic torque is introduced into the ferrofluid, which consists  
17  
18 of colloidally stabilized magnetic nanoparticles (typically magnetite) suspended in a non-  
19  
20 magnetizable liquid, through the misalignment of the particle's permanent magnetization and the  
21  
22 applied rotating magnetic field. The internal angular momentum of a continuum ferrofluid  
23  
24 'parcel' (containing a representative collection of liquid molecules and rotating magnetic  
25  
26 nanoparticles) becomes significant and the continuum stress tensor becomes anti-symmetric for  
27  
28 strong enough magnetic body torques introduced at the microscopic level. A moment-of-inertia  
29  
30 density is defined for the ferrofluid parcel based on the mass distributions of the liquid molecules  
31  
32 and magnetic particles in the parcel. A continuum spin velocity (column vector) is then defined  
33  
34 by the product of the internal angular momentum density (column vector) with the inverse of the  
35  
36 moment-of-inertia density (tensor) [28-30]. Since a ferrofluid continuum contains an enormous  
37  
38 amount of these parcels, the spin velocity,  $\bar{\omega}$ , is defined as a continuous field quantity which in  
39  
40 general, can be a function of space and time, *i.e.*,  $\bar{\omega} = \bar{\omega}(x, y, z, t)$ . In order to describe how  
41  
42 microscopic particle rotation affects the continuum flow motion, a continuum angular  
43  
44 momentum conservation equation is added and coupled with the linear momentum equation so  
45  
46 that, in general, the externally applied magnetic body couple, angular momentum conversion  
47  
48 between linear and spin velocity fields, and the diffusive transport of angular momentum are  
49  
50 incorporated into the description of the flow momentum balances [22, 28-31].

51  
52 A fundamental issue in the current development of ferrofluid spin-up flow is whether the  
53  
54 diffusive angular momentum transport or couple stress has a finite contribution to the angular  
55  
56 momentum balances of the flow. The current consensus is that the couple stress contribution is  
57  
58 vanishingly small, *i.e.*, zero spin viscosity or diffusive transport conditions, as discussed in  
59  
60 Rosensweig [22], Chaves *et al.* [26, 27], and Schumacher *et al.* [32]. In a most recent work by  
61  
62 Feng *et al.* [33], scaling and numerical analyses were presented to show that in the limit of an  
63  
64 effective continuum, the angular momentum equation is to be couple stress free and the value of  
65

1  
2  
3  
4 the spin viscosity should be identically zero. However, spin-up velocity profiles measured by  
5 ultrasound velocimetry reported by He [23], Elborai [24], and Chaves *et al.* [26, 27] were  
6 compared with the numerical simulations of the full spin-up flow governing equations and found  
7 that the experimental and numerical results would agree only if the spin viscosity assumes some  
8 finite value instead of being vanishingly small or identically zero.  
9

10  
11 Acknowledging the experimental and theoretical discrepancies in the value of spin viscosity  
12 and identifying the “mathematically analogous, physically parallel mechanisms” governing the  
13 respective electrorotation and ferrofluid spin-up flows as summarized in Table 1, this work is  
14 therefore aimed at developing a classical continuum mechanical model that combines particle  
15 electrorotation and anti-symmetric/couple stress theories for describing the electrorheological  
16 behavior of a particle-liquid mixture (termed ER fluid henceforward) subjected to a DC electric  
17 field strength higher than the Quincke rotation threshold in both Couette and Poiseuille flow  
18 geometries. Using a set of continuum modeling field equations similar to that utilized in  
19 ferrofluid spin-up flow analyses, we investigate the effects of a zero spin viscosity,  $\eta' = 0$ , *i.e.*,  
20 zero diffusive transport of angular momentum or couple stress free conditions, on the angular  
21 momentum balances in the present negative ER fluid flow of interest. In the next section, the  
22 governing equations describing the mass conservation, linear momentum conservation, angular  
23 momentum conservation, and polarization relaxation of the ER fluid flow will be given in their  
24 most general forms. The specific governing equations, analytical expressions of the spin velocity  
25 solutions, and the evaluated numerical results are then presented, compared, and discussed in  
26 Sections 3 and 4 to respectively show how the pertinent physical parameters are related to the ER  
27 responses and fluid flow for two dimensional (2D) Couette and Poiseuille flows with internal  
28 micro-particle electrorotation. A conclusion is given at the end of this article to summarize the  
29 principle findings and the motivations for future research.  
30  
31  
32  
33  
34  
35  
36  
37  
38  
39  
40  
41  
42  
43  
44  
45  
46  
47  
48  
49  
50  
51

## 52 **2. General Formulation**

53  
54 In order to quantitatively model and describe the present ER flow phenomenon, several  
55 physical principles involved are considered: (i) the continuity or mass conservation, (ii) the linear  
56 momentum balance, (iii) the angular momentum balance, and (iv) the polarization relaxation of  
57  
58  
59  
60  
61  
62  
63  
64  
65

the ER fluid flow. The governing equations are given in the following subsections to describe the above physical principles in proper mathematical forms.

### 2.1 The Fluid Mechanical Equations

The continuum equations describing the ER fluid motion are the mass continuity equation for incompressible flow,

$$\nabla \cdot \bar{v} = 0, \quad (2)$$

the linear momentum equation,

$$\rho \frac{D\bar{v}}{Dt} = -\nabla p + (\bar{P}_t \cdot \nabla) \bar{E} + 2\zeta \nabla \times \bar{\omega} + \beta \nabla (\nabla \cdot \bar{v}) + \eta_e \nabla^2 \bar{v}, \quad (3)$$

and the angular momentum equation,

$$I \frac{D\bar{\omega}}{Dt} = \bar{P}_t \times \bar{E} + 2\zeta (\nabla \times \bar{v} - 2\bar{\omega}) + \beta' \nabla (\nabla \cdot \bar{\omega}) + \eta' \nabla^2 \bar{\omega}, \quad (4)$$

where  $\bar{v}$  is the linear flow velocity,  $\rho$  is the ER fluid density,  $p$  is the hydrodynamic pressure in the flow field,  $\bar{P}_t$  is the fluid total polarization,  $\bar{E}$  is the electric field,  $\bar{\omega}$  is the flow spin velocity,  $I$  is the average moment of inertia per unit volume,  $\eta'$  is the spin viscosity,  $\zeta$  is the vortex viscosity which is related to the carrier liquid viscosity,  $\eta_0$ , and particle solid volume fraction,  $\phi$ , through  $\zeta \sim 1.5\phi\eta_0$  for dilute suspensions with  $\phi \ll 1$ ,  $\beta = \lambda + \eta - \zeta$  is the sum of the second coefficient of viscosity,  $\lambda$ , the zero field ER fluid viscosity,  $\eta \sim \eta_0(1 + 2.5\phi)$ , and the negative of the vortex viscosity,  $\eta_e = \eta + \zeta$  is the sum of the zero field ER fluid viscosity and the vortex viscosity,  $\beta' = \eta' + \lambda'$  is the sum of the spin viscosity and the second coefficient of spin viscosity,  $\lambda'$  [19, 22, 30], and  $D/Dt$  is the material derivative given by

$$\frac{D}{Dt} = \frac{\partial}{\partial t} + (\bar{v} \cdot \nabla). \quad (5)$$

Note that Eq. (3) generally follows the form of the well known Navier-Stokes equation. However, by introducing micro-particle rotation to the fluid flow, additional terms are included in Eq. (3) to account for the Kelvin body force density,  $(\bar{P}_t \cdot \nabla) \bar{E}$ , and the anti-symmetric force density,  $2\zeta \nabla \times \bar{\omega}$ , as contributions in the linear momentum balances of the fluid flow. Moreover, Eq. (4) characterizes the ER fluid parcel spin velocity,  $\bar{\omega}$ , so that the torque and angular

1  
2  
3  
4 momentum balances resulting from the electrical torque input and fluid motion can be described  
5 and related to other variables pertinent to this problem. In Eq. (4), the left hand side represents  
6 the angular momentum per unit volume of a continuum ER fluid parcel; the first term on the  
7 right hand side (RHS) represents the electrical torque density introduced to the flow field via the  
8 rotating micro-particles under the action of the external DC field; the second term on the RHS  
9 represents the angular momentum density transformation or conversion between the vorticity and  
10 the spin velocity fields; the third term on the RHS represents the gradient of the divergence of  
11 the spin velocity and is analogous to the “gradient of the divergence of the velocity” term in Eq.  
12 (3) that measures the bulk compression effects in the fluid flow; and finally, the last term on the  
13 RHS represents the diffusive transport of angular momentum within the flow field [22].  
14  
15  
16  
17  
18  
19  
20  
21  
22  
23

## 24 *2.2 The Equilibrium Polarization and Polarization Relaxation Equations*

25  
26 The electric field in the ER flow field is generally described by the electro-quasi-static (EQS)  
27 Maxwell equations [16, 34], namely,  
28

$$29 \nabla \times \bar{E} \approx 0, \text{ and} \tag{6}$$

$$30 \nabla \cdot \bar{D} = \rho_f \approx 0, \tag{7}$$

31  
32 where  $\bar{D}$  is the electric displacement field and  $\rho_f$  is the free space charge density. Here, we  
33 have assumed that on the macroscopic continuum level, the free space charge density is zero.  
34  
35  
36  
37

38 To complete the description of the electrical subsystem, we need a continuum  
39 phenomenological polarization relaxation equation that accounts for the non-equilibrium effects  
40 of both the linear and angular motions on the ER fluid polarization. Since the torque input on the  
41 micro scale is related to the induced surface charge around the surface of the micro-particles, we  
42 shall focus on how non-equilibrium motion, *i.e.*, micro-particle rotation,  $\bar{\Omega}$ , continuum fluid  
43 spin velocity,  $\bar{\omega}$ , and continuum fluid velocity,  $\bar{v}$ , affects the *retarding polarization*,  $\bar{P}$  (the part  
44 of polarization directly related to the surface charges [7-12]), instead of the total polarization of  
45 the ER fluid,  $\bar{P}_t$ . Note that by definition, the spin velocity,  $\bar{\omega}$ , and the linear velocity,  $\bar{v}$ , are  
46 continuum variables which are related to respective averages of the internal angular momentum  
47 and linear momentum over collections of micro-particles and carrier liquid molecules in an ER  
48 fluid parcel. They should be distinguished from the micro-particle rotation velocity,  $\bar{\Omega}$ , which is  
49 the microscopic angular velocity of the suspended micro-particles within an ER fluid parcel.  
50  
51  
52  
53  
54  
55  
56  
57  
58  
59  
60  
61  
62  
63  
64  
65

We start the development of the polarization relaxation equation and its equilibrium polarization from the micro scale. The governing equation for the two region problem of the EQS fields within ( $r < R$ ) and outside ( $r > R$ ) a spherical solid particle suspended in a liquid medium rotating at a constant speed,  $\bar{\Omega} = \Omega \bar{i}_x$ , subjected to a uniform electric field,  $\bar{E}^\dagger = E_z^\dagger \bar{i}_z = E_0 \bar{i}_z$  ( $\dagger$  denotes microscopic field quantities), as shown in Fig. 1 is the Laplace's equation in spherical coordinates,

$$\nabla^2 \Phi^\dagger = \frac{1}{r^2} \frac{\partial}{\partial r} \left( r^2 \frac{\partial \Phi^\dagger}{\partial r} \right) + \frac{1}{r^2 \sin \theta} \frac{\partial}{\partial \theta} \left( \sin \theta \frac{\partial \Phi^\dagger}{\partial \theta} \right) + \frac{1}{r^2 \sin^2 \theta} \frac{\partial^2 \Phi^\dagger}{\partial \phi^2} = 0, \quad (8)$$

where  $R$  is the radius of the micro-particle and  $\Phi^\dagger$  is the electric potential, *i.e.*,  $\bar{E}^\dagger = -\nabla \Phi^\dagger$ . The boundary conditions on Eq. (8) are the electric field strength far away from the micro-particle,

$$\bar{E}^\dagger \rightarrow E_0 \bar{i}_z = E_0 (\cos \theta \bar{i}_r - \sin \theta \bar{i}_\theta) \text{ as } r \rightarrow \infty, \quad (9a)$$

the continuity of the electric potential at the solid-liquid interface,

$$\Phi^\dagger (r = R^-, \theta, \phi) = \Phi^\dagger (r = R^+, \theta, \phi), \quad (9b)$$

and charge conservation at the rotating micro-particle surface,

$$\bar{n} \cdot \left[ \bar{J}_f^\dagger \right] + \nabla_\Sigma \cdot \bar{K}_f^\dagger = 0 \text{ at } r = R, \quad (9c)$$

in which  $\bar{n} = \bar{i}_r$  is the normal vector of the spherical surface,  $\bar{J}_f^\dagger = \sigma \bar{E}^\dagger$  is the Ohmic current per unit area,  $\bar{n} \cdot \left[ \bar{J}_f^\dagger \right] = \sigma_1 E_r^\dagger (r = R^+, \theta, \phi) - \sigma_2 E_r^\dagger (r = R^-, \theta, \phi)$  with  $E_r^\dagger$  being the  $r$  component of the electric field,  $\nabla_\Sigma = (\bar{I} - \bar{n}\bar{n}) \cdot \nabla$  is the surface divergence, and  $\bar{K}_f^\dagger = \sigma_f \bar{V}$  is the surface current density with  $\sigma_f = \varepsilon_1 E_r^\dagger (r = R^+, \theta, \phi) - \varepsilon_2 E_r^\dagger (r = R^-, \theta, \phi)$  and  $\bar{V} = \Omega \bar{i}_x \times R \bar{i}_r = -\Omega R \cdot (\sin \phi \bar{i}_\theta + \cos \theta \cos \phi \bar{i}_\phi)$ . Using Eqs. (8) and (9), the electric potentials and electric fields within and outside the rotating micro-particle can be solved by the method of separation of variables with the aid of associated Legendre polynomials. This problem has been solved by Cebers [35]; here, we only summarize the solutions to the electric potential and the effective dipole moment of the particle for  $r > R$ . The outer electric potential ( $r > R$ ) is given in spherical coordinates as



$$\Phi^\dagger(r, \theta, \phi) = -rE_0 \cos \theta + \frac{\overline{p}_t^\dagger \cdot \overline{i}_r}{4\pi\epsilon_1 r^2} = -rE_0 \cos \theta + \frac{4\pi\epsilon_1}{4\pi\epsilon_1 r^2} (a_3 \cos \theta + a_6 \sin \phi \sin \theta), \quad (10)$$

where

$$a_3 = E_0 R^3 \left[ \frac{\epsilon_2 - \epsilon_1}{2\epsilon_1 + \epsilon_2} + \frac{\left( \frac{\sigma_2 - \sigma_1}{2\sigma_1 + \sigma_2} - \frac{\epsilon_2 - \epsilon_1}{2\epsilon_1 + \epsilon_2} \right)}{1 + \tau_{MW}^2 \Omega^2} \right], \quad (11)$$

$$a_6 = -E_0 R^3 \frac{\left( \frac{\sigma_2 - \sigma_1}{2\sigma_1 + \sigma_2} - \frac{\epsilon_2 - \epsilon_1}{2\epsilon_1 + \epsilon_2} \right) \tau_{MW} \Omega}{1 + \tau_{MW}^2 \Omega^2}, \quad (12)$$

$$\overline{p}_t^\dagger = p_x^\dagger \overline{i}_x + p_y^\dagger \overline{i}_y + p_z^\dagger \overline{i}_z, \quad (13)$$

$$\overline{i}_r = \sin \theta \cos \phi \overline{i}_x + \sin \theta \sin \phi \overline{i}_y + \cos \theta \overline{i}_z, \quad (14)$$

and

$$\tau_{MW} \equiv \frac{2\epsilon_1 + \epsilon_2}{2\sigma_1 + \sigma_2}, \quad (15)$$

is the Maxwell-Wagner relaxation time. With Eqs. (10)-(14), we can find the total dipole moment of the rotating particle,  $\overline{p}_t^\dagger$ , as  $p_x^\dagger = 0$ ,  $p_y^\dagger = 4\pi\epsilon_1 a_6$ , and  $p_z^\dagger = 4\pi\epsilon_1 a_3$ , and the *retarding part* of the dipole moment is then found as

$$\overline{p}^\dagger = 4\pi\epsilon_1 a_6 \overline{i}_y + 4\pi\epsilon_1 \left( a_3 - E_0 R^3 \frac{\epsilon_2 - \epsilon_1}{2\epsilon_1 + \epsilon_2} \right) \overline{i}_z. \quad (16)$$

The surface charge around the spherical particle with half of the hemisphere having positive charge and the other half having negative charge is directly related to the retarding dipole moment given by Eq. (16) [35]. By applying a torque balance between the electric torque,  $\overline{p}_t^\dagger \times \overline{E}^\dagger = \overline{p}^\dagger \times \overline{E}^\dagger = 4\pi\epsilon_1 a_6 E_0 \overline{i}_x$ , and the viscous torque,  $-8\pi\eta_0 \Omega R^3 \overline{i}_x$ , on the particle in steady state, we can find the critical electric field for Quincke rotation as given in Eq. (1) and the rotation velocity of the micro-particle being [18]

$$\Omega = \begin{cases} \pm \frac{1}{\tau_{MW}} \sqrt{\left(\frac{E_0}{E_c}\right)^2 - 1}, & E_0 \geq E_c, \\ 0, & E_0 < E_c \end{cases}, \quad (17)$$

where the + and - signs denote counter clockwise and clockwise rotation with the coordinate system defined in Fig. 1. In Eq. (17), we have assumed that the particle rotation is only in the  $x$ -direction; this is because we will only be considering 2D flow geometries in the following discussions. Note however that for the most general cases, the particle rotation axis is perpendicular to the planes defined by the electric field, which has a three dimensional feature.

We next consider a dilute particle suspension with a solid volume fraction of  $\phi$  and a particle number density of  $n$  subjected to the DC electric field. The solid volume fraction and the particle number density are related through

$$\phi = n \left( \frac{\pi d^3}{6} \right) \sim O(nR^3), \quad (18)$$

where  $d = 2R$  is the diameter of the micro-particle. Assuming that the mutual electrical interactions between the suspended micro-particles can be neglected (*i.e.*, dilute suspension with  $\phi \ll 1$ ), the macroscopic *retarding* polarization of the ER fluid at equilibrium,  $\overline{P}_{eq}$ , can be obtained by multiplying Eq. (16) with the particle number density,  $n$ , *i.e.*,  $\overline{P}_{eq} = n \overline{p}^\dagger =$

$P_{eq}^y \overline{i}_y + P_{eq}^z \overline{i}_z$ , with

$$\begin{bmatrix} P_{eq}^y \\ P_{eq}^z \end{bmatrix} = 4\pi\epsilon_1 n R^3 \begin{bmatrix} \tau_{MW} \Omega \left( \frac{\sigma_2 - \sigma_1}{2\sigma_1 + \sigma_2} - \frac{\epsilon_2 - \epsilon_1}{2\epsilon_1 + \epsilon_2} \right) \\ \frac{\left( \frac{\sigma_2 - \sigma_1}{2\sigma_1 + \sigma_2} - \frac{\epsilon_2 - \epsilon_1}{2\epsilon_1 + \epsilon_2} \right)}{1 + \tau_{MW}^2 \Omega^2} \end{bmatrix} E_0. \quad (19)$$

Equation (19) represents the macroscopic retarding polarization of a static, motionless ER fluid, namely,  $\overline{\omega} = 0$  and  $\overline{v} = 0$ . However, this does not mean that at macroscopic equilibrium, the micro-particles cannot rotate on the microscopic level, *i.e.*,  $\overline{\Omega} \neq 0$ , when the applied electric field is larger than the critical electric field given in Eq. (1), that is,  $E_0 \geq E_c$ . This formulation is similar to the dynamic effective medium model shown by Xiao *et al.* [36]. As for the cases of

1  
2  
3  
4  $E_0 < E_c$ ,  $\Omega$  is set to zero in Eq. (19) since an applied field less than the critical field will give  
5  
6 imaginary values of  $\Omega$  and the real root can only be zero as in Eq. (17). Note that by setting the  
7  
8 micro-particle rotation speed  $\Omega$  to zero, the equilibrium retarding polarization shown in Eq. (19)  
9  
10 reduces back to the one given by Cebers [35], *i.e.*, all micro-particle rotation speed, continuum  
11  
12 linear velocity, and continuum spin velocity equal to zero. Combining Eqs. (17) and (19) and  
13  
14 extending the physical arguments of the phenomenological magnetization relaxation equation  
15  
16 proposed by Shliomis [22, 37, 38] to the case of the retarding polarization, we arrive at the  
17  
18 following retarding polarization relaxation equation,

$$\frac{D\bar{P}}{Dt} = (\bar{\omega} \times \bar{P}) - \frac{1}{\tau_{MW}} (\bar{P} - \bar{P}_{eq}), \quad (20)$$

19  
20  
21  
22  
23 where  $\bar{P}$  is the retarding polarization.

24  
25 Equations (17), (19), and (20) account for the non-equilibrium effects of the micro-particle  
26  
27 rotation velocity,  $\bar{\Omega}$ , ER fluid spin velocity,  $\bar{\omega}$ , and ER fluid linear velocity,  $\bar{v}$ , on the retarding  
28  
29 polarization. In the development of Eqs. (17), (19), and (20), we have assumed that the induced  
30  
31 dipole moment on the micro-particles obeys the Maxwell-Wagner polarization—the induced  
32  
33 charges are distributed on the surface of the particles at the micro scale. We have also assumed  
34  
35 that only the retarding part of the macroscopic ER fluid polarization, *i.e.*, the polarization directly  
36  
37 related to the interfacial charges, needs to be relaxed according to the non-equilibrium motions.  
38  
39 Unlike the ferrofluid equilibrium magnetization, the equilibrium retarding polarization, Eq. (19),  
40  
41 does not follow a Langevin function [22]. This is because we are considering the rotation of  
42  
43 micro-sized dielectric insulating particles on which Brownian motion has little influence [18].  
44  
45 Rigorously speaking, the micro-particle rotation speed,  $\Omega$ , that enters Eqs. (19) and (20) should  
46  
47 be the speed observed in the reference frame that rotates with the ER fluid parcel. Yet, the  
48  
49 mathematical analysis of this ER fluid flow will become much more involved and impractical in  
50  
51 attempts to correct for the difference in reference frames, and is beyond the scope of this work.  
52  
53 As a first approach, we employ Eq. (17) in Eqs. (19) and (20) to incorporate both microscopic  
54  
55 (*i.e.*,  $\bar{\Omega}$ ) and macroscopic (*i.e.*,  $\bar{\omega}$  and  $\bar{v}$ ) motions under one continuum mechanical framework.  
56  
57  
58  
59  
60  
61  
62  
63  
64  
65

### 3. Couette Flow with Internal Micro-particle Electrorotation

#### 3.1 The Governing Equations Specific to the Couette Flow Geometry

Consider the Couette flow geometry shown in the schematic diagram of Fig. 2. The lower plate of the parallel plate system is fixed at zero velocity while the upper plate is applied with a constant velocity,  $U_0$ , in the positive  $y$ -direction. We assume that the flow is steady ( $\partial/\partial t = 0$ ), incompressible, fully developed ( $\partial/\partial y = 0$ ), and two-dimensional ( $\partial/\partial x = 0$ ) in Cartesian coordinates. Under these assumptions, the continuity equation, Eq. (2), with  $\bar{v} = u_y \bar{i}_y + u_z \bar{i}_z$  is readily reduced to  $du_z/dz = 0$  and subsequently to  $u_z = 0$  since the  $z$ -velocity component,  $u_z$ , has to satisfy the no-slip and non-penetrating (impermeable walls) boundary conditions at  $z = 0$  and  $h$  with  $h$  being the height of the 2D channel. Moreover, by using the EQS Faraday's equation, Eq. (6), with  $\bar{E} = E_y \bar{i}_y + E_z \bar{i}_z$  and the condition of fully developed flow, we find  $dE_y/dz = 0$  such that  $E_y$  is just a constant throughout the 2D channel. Noting that the boundaries at  $z = 0$  and  $h$  are perfectly conducting electrodes, and that the tangential component of the electric field is continuous across the boundaries, the constant  $E_y$  is simply zero. Therefore, the applied DC electric field is to be in the  $z$ -direction only. The fringing effects at the ends of the channel are to be neglected.

The governing equations are further simplified by considering a zero spin viscosity, *i.e.*,  $\eta' = 0$ , in the angular momentum equation, Eq. (4). Given the above assumptions combined with the continuity and zero spin viscosity conditions, Eqs. (3), (4), and (20), are then simplified into the following:

$$-\tau_{MW} \omega_x P_z - (P_y - P_{eq}^y) = 0, \quad (21a)$$

$$\tau_{MW} \omega_x P_y - (P_z - P_{eq}^z) = 0, \quad (21b)$$

$$2\zeta \frac{d\omega_x}{dz} + \eta_e \frac{d^2 u_y}{dz^2} = 0, \quad (22)$$

and

$$P_y E_z + 2\zeta \left( -\frac{du_y}{dz} - 2\omega_x \right) = 0, \quad (23)$$

where  $u_y$  is the  $y$ -velocity component,  $\omega_x$  is the  $x$ -spin velocity component (note:  $\bar{\omega} = \omega_x \bar{i}_x$  in

2D),  $E_z$  is the  $z$ -component of the applied DC electric field, and  $P_y$  and  $P_z$  are respectively the retarding polarization components in the  $y$ - and  $z$ - directions, *i.e.*,  $\bar{P} = P_y \bar{i}_y + P_z \bar{i}_z$ . Note that we have substituted the total polarization,  $P_{ty}$ , with the retarding polarization,  $P_y$ , in Eq. (23). This is because the DC electric field is applied in the  $z$ -direction only with  $E_y = 0$ . Thus the total polarization in the  $y$ -direction comes from the dipole moment tilt of the rotating micro-particles in the micro scale, which, on the macroscopic level, is generally the  $y$ -component of the retarding polarization. Finally, the  $z$ -linear momentum equation reduces to an equation which relates only the pressure gradient to the Kelvin body force density, and thus can be treated separately from the other equations.

Substituting Eq. (19) into Eq. (21), we can solve for the  $y$ - and  $z$ - components of the retarding polarization as

$$P_y = n \frac{\alpha_y - \tau_{MW} \omega_x \alpha_z}{1 + \tau_{MW}^2 \omega_x^2} E_0, \quad (24a)$$

$$P_z = n \frac{\alpha_z + \tau_{MW} \omega_x \alpha_y}{1 + \tau_{MW}^2 \omega_x^2} E_0, \quad (24b)$$

where

$$\begin{bmatrix} \alpha_y \\ \alpha_z \end{bmatrix} = 4\pi\epsilon_1 R^3 \begin{bmatrix} \tau_{MW} \Omega \left( \frac{\sigma_2 - \sigma_1}{2\sigma_1 + \sigma_2} - \frac{\epsilon_2 - \epsilon_1}{2\epsilon_1 + \epsilon_2} \right) \\ \frac{\left( \frac{\sigma_2 - \sigma_1}{2\sigma_1 + \sigma_2} - \frac{\epsilon_2 - \epsilon_1}{2\epsilon_1 + \epsilon_2} \right)}{1 + \tau_{MW}^2 \Omega^2} \end{bmatrix}, \quad (25)$$

with  $\Omega$  given in Eq. (17). Generally speaking, the  $z$ -component of the electric field,  $E_z$ , in Eq. (23) depends on the flow linear and spin velocities, and the EQS equations, Eqs. (6) and (7), need to be solved together with the retarding polarization, Eqs. (24) and (25), linear momentum, Eq. (22), and angular momentum, Eq. (23), equations with the suitable electrical and mechanical boundary conditions applied at  $z=0$  and  $h$ . However, the coupled set of governing equations becomes much more non-linear and less practical for engineering analysis purposes. Assuming that, due to flow motion, corrections to the  $z$ -electric field,  $E_z$ , can be related to the microscopic applied electric field and the micro-particle solid volume fraction through

$$E_z \sim E_z^\dagger + \phi e_1 + \phi^2 e_2 + \dots \sim E_0 + \phi e_1 + \phi^2 e_2 + \dots, \quad (26)$$

where  $e_i$ 's are the correction terms, we substitute Eq. (24a) into Eq. (23) and approximate to the first order of magnitude of the volume fraction,  $\phi$ ,  $E_z \approx E_0 + \phi e_1 + \dots$  for dilute suspensions, *i.e.*,  $\phi \ll 1$ , so that the electrical field equations, Eqs. (6) and (7), can be decoupled from the mechanical field equations, Eqs. (2)-(4), or Eqs. (22) and (23). Hence the governing equations specific to the Couette flow geometry with internal particle electrorotation is obtained as Eq. (22) and

$$\frac{\alpha^* - \tau_{MW} \omega_x}{1 + \tau_{MW}^2 \omega_x^2} n \alpha_z E_0^2 + 2\zeta \left( -\frac{du_y}{dz} - 2\omega_x \right) = 0. \quad (27)$$

where  $\alpha^* = \alpha_y / \alpha_z = -\tau_{MW} \Omega$ . In Eq. (27), the first  $\alpha$  order correction,  $e_1$ , to the  $z$ -electric field has been neglected because  $e_1$  has become a second order term after being substituted into Eq. (23), *i.e.*,  $n \alpha_z E_0 E_z \approx n \alpha_z E_0 (E_0 + \phi e_1 + \dots)$  with  $\phi \ll 1$  and  $n \alpha_z \sim n R^3 \sim n d^3 \sim O(\phi)$  as in Eq. (18). The boundary condition for the velocity field,  $\bar{v} = u_y \bar{i}_y$ , is the general no-slip boundary condition, *i.e.*,  $\bar{v} = 0$  at  $z = 0$  and  $\bar{v} = U_0 \bar{i}_y$  at  $z = h$ . On the other hand, the angular momentum equation, Eq. (27), eventually reduces to an algebraic equation for zero spin viscosity conditions as will be discussed shortly in Section 3.2; hence, there are no additional constraints to be applied at the boundaries for the Couette spin velocity field. This “free-to-spin” condition on  $\omega_x$  for  $\eta' = 0$  is likely an analogous case to the Euler equation for inviscid fluid flow—the linear flow velocity is allowed to slip at the solid-fluid boundaries when the fluid viscosity goes to zero.

### 3.2 Solutions to the Spin Velocity and Effective Viscosity

Integrating Eq. (27) with respect to  $z$ , we have

$$2\zeta \omega_x + \eta_e \frac{du_y}{dz} = C_c, \quad (28)$$

where  $C_c$  is a constant. Substituting Eq. (28) into Eq. (27), we find that the spin velocity,  $\omega_x$ , does not depend on the spatial coordinate,  $z$ , and therefore Eq. (22) reduces to the original governing equation for simple Couette flow, *i.e.*,

$$\frac{d^2 u_y}{dz^2} = 0, \quad (29)$$

and the solution to Eq. (29) is

$$u_y(z) = \frac{U_0}{h} z. \quad (30)$$

Inserting Eq. (30) into Eq. (27) and using the following non-dimensionalization scheme, namely,

$$\omega^* = \tau_{MW} \omega_x, \quad \gamma^* = \tau_{MW} \frac{U_0}{h}, \quad \text{and} \quad M^* = \frac{2\zeta}{n\alpha_z E_0^2 \tau_{MW}}, \quad (31)$$

the non-dimensional angular momentum equation is obtained as

$$\omega^{*3} + \frac{\gamma^*}{2} \omega^{*2} + \left(1 + \frac{1}{2M^*}\right) \omega^* + \left(\frac{\gamma^*}{2} - \frac{\alpha^*}{2M^*}\right) = 0. \quad (32)$$

Equation (32) can be solved to obtain analytical expressions by symbolic calculation packages (Mathematica, Wolfram Research, Inc.) and the three roots of Eq. (32) are expressed as functions of  $\gamma^*$  and  $M^*$ . Nevertheless, it should be pointed out that not all the three roots to  $\omega^*$  are likely to be physically meaningful and interpretable for the flow phenomena of interest presented herein. Moreover, each of the three roots may vary from real to complex valued (or vice versa) in different parametric regimes. In order to find the most physically meaningful and interpretable solution or combination of solutions from the three possible roots to the current problem, the following considerations and conditions are applied to the flow field: (i) only real valued solutions are considered, (ii) the ER fluid is “free-to-spin” at the solid-ER fluid boundaries since the governing physics reduce from a boundary value problem to an algebraic problem in zero spin viscosity conditions, and (iii) due to micro scale viscous interactions, the micro-particle angular velocity,  $\bar{\Omega}$ , should rotate in the same direction as that of the macroscopic ER flow vorticity so that the micro-particle rotation is always stable [7-12].

We have shown that the spin velocity is a constant throughout the channel when  $\eta' = 0$  in the Couette geometry. Hence,  $\omega^*$  assumes some finite value at the solid-ER fluid boundaries, which is readily self-consistent with the “free-to-spin” condition. To satisfy condition (iii) for  $E_0 \geq E_c$ , we need to substitute into Eqs. (24) and (25) the micro-particle angular velocity with the minus sign in Eq. (17) which has the same negative sign (or clockwise rotation) as the macroscale Couette flow vorticity, namely,  $\nabla \times \bar{v} = -\left(\frac{du_y}{dz}\right) \bar{i}_x = -(U_0/h) \bar{i}_x$ , with the coordinate systems

defined in Figs. 1 and 2. For  $E_0 < E_c$ , we employ  $\Omega = 0$  (see Eq. (17)) in Eqs. (24) and (25) and pick out or select the root to the spin velocity,  $\omega^*$  or  $\omega_x$ , that has the same negative sign as the Couette flow vorticity. For the parametric regimes of our interests, we identify the stable and real valued solution to the spin velocity as: for  $E_0 \geq E_c$  (use negative  $\Omega$  value in Eqs. (17), (24), and (25)),

$$\omega_{c2}^* = -\frac{\gamma^*}{6} - \varphi_{c1} (1+i\sqrt{3}) \left[ 6^3 \sqrt{4M^*} \left( \varphi_{c2} + \sqrt{4\varphi_{c1}^3 + \varphi_{c2}^2} \right)^{1/3} \right]^{-1} + \frac{1}{12^3 \sqrt{2M^*}} \left[ (1-i\sqrt{3}) \left( \varphi_{c2} + \sqrt{4\varphi_{c1}^3 + \varphi_{c2}^2} \right)^{1/3} \right], \quad (33)$$

for  $E_0 \leq 0.8E_c$  (use  $\Omega = 0$  in Eqs. (17), (24), and (25)),

$$\omega_{c1}^* = -\frac{\gamma^*}{6} + \varphi_{c1} \left[ 3^3 \sqrt{4M^*} \left( \varphi_{c2} + \sqrt{4\varphi_{c1}^3 + \varphi_{c2}^2} \right)^{1/3} \right]^{-1} - \frac{1}{6^3 \sqrt{2M^*}} \left( \varphi_{c2} + \sqrt{4\varphi_{c1}^3 + \varphi_{c2}^2} \right)^{1/3}, \quad (34)$$

and for  $0.8E_c < E_0 < E_c$  with  $\Omega = 0$  in Eqs. (17), (24), and (25),  $\omega^*$  is given by both  $\omega_{c1}^*$  and  $\omega_{c2}^*$ , *i.e.*, Eqs. (33) and (34), where

$$\varphi_{c1} = 6M^* + 12M^{*2} - M^{*2}\gamma^{*2}, \quad (35)$$

and

$$\varphi_{c2} = -18M^{*2}\gamma^* + 72M^{*3}\gamma^{*2} + 2M^{*3}\gamma^{*3} - 108M^{*2}\alpha^*. \quad (36)$$

Note that the results shown in Eqs. (33)-(36) are obtained under the ‘‘Solve’’ command of Mathematica. In  $0.8E_c < E_0 < E_c$ , part of the real valued solution to  $\omega^*$  is given by Eq. (33) and the other part is given by Eq. (34), thus, both solutions have to be used in the evaluation of the spin velocity solutions.

The effective viscosity of Couette flows with particle electrorotation,  $\eta_{eff}$ , is derived by recognizing the relationship between the wall shear stress,  $\tau_s$ , and the average shear rate (or the velocity of the upper plate,  $U_0$ , divided by the channel height,  $h$ ) when the shear stress is held constant for a given flow or experimental condition, *i.e.*,

$$\tau_s = \eta_{eff} \frac{U_0}{h} = \eta_{eff} \frac{\gamma^*}{\tau_{MW}} = \bar{i}_z \cdot \left[ \overline{\overline{T}} \right] \cdot \bar{i}_y, \quad (37a)$$

in which  $\bar{i}_z$  denotes the shear stress differences across the solid-liquid interface,  $\bar{i}_z$  is the row



vector  $[0 \ 0 \ 1]$ ,  $\bar{i}_y$  is the column vector  $[0 \ 1 \ 0]^t$ , and  $\bar{\bar{T}} = \bar{\bar{T}}_s + \bar{\bar{T}}_a$  is the total stress tensor with the symmetric part being

$$\bar{\bar{T}}_s = -p\bar{\bar{I}} + \eta \left[ \nabla \bar{v} + (\nabla \bar{v})^t \right] = \begin{bmatrix} -p & 0 & 0 \\ 0 & -p & \eta \frac{du_y}{dz} \\ 0 & \eta \frac{du_y}{dz} & -p \end{bmatrix}, \quad (37b)$$

and the anti-symmetric part being

$$\bar{\bar{T}}_a = \zeta \bar{\bar{\varepsilon}} \cdot (\nabla \times \bar{v} - 2\bar{\omega}) = \begin{bmatrix} 0 & 0 & 0 \\ 0 & 0 & \zeta \left( -\frac{du_y}{dz} - 2\omega_x \right) \\ 0 & -\zeta \left( -\frac{du_y}{dz} - 2\omega_x \right) & 0 \end{bmatrix}, \quad (37c)$$

[22]. By expanding the total stress tensor into matrix form as in Eqs. (37b) and (37c) and substituting the velocity field, Eq. (30), and the spin velocity field, Eq. (33) and/or (34), into Eq. (37), the effective viscosity defined in Eq. (37a) can be obtained as

$$\eta_{eff} = \eta_e + 2\zeta \frac{\omega^*}{\gamma^*}, \quad (38a)$$

or in dimensionless terms,

$$\eta^* \equiv \frac{\eta_{eff}}{\eta} = \frac{\eta_e}{\eta} + \frac{2\zeta}{\eta} \frac{\omega_{Ci}^*}{\gamma^*}, \quad (38b)$$

where  $\omega_{Ci}^* = \omega_{C1}^*$  and/or  $\omega_{C2}^*$  depending on the regimes of the electric field strength where  $\omega_{Ci}^*$  become real valued, and  $\eta \approx \eta_0(1+2.5\phi)$  is the zero field ER fluid (particle-liquid mixture) viscosity as defined in Section 2.1. The shear stress difference in Eq. (37a) is evaluated at  $z=0$ .

### 3.3 Results and Discussions

After obtaining the velocity and spin velocity fields as well as the effective viscosity, we now further present the numerical evaluations of the analytical expressions given in Eqs. (33), (34), and (38). The system parameters, physical constants, and material properties used in our

1  
2  
3  
4 evaluations follow those given in Ref. [7-12] so as to facilitate a more effective comparison  
5  
6 between the current continuum model and the two-phase effective continuum formulation found  
7  
8 in the literature. These data are summarized in Table 2.

9  
10 Shown in Fig. 3 is the Couette spin velocity,  $\omega^* = \tau_{MW}\omega_x$ , given by Eq. (33), *i.e.*,  $\omega^* = \omega_{C2}^*$ ,  
11  
12 for  $E_0 \geq E_c$  and by Eq. (34), *i.e.*,  $\omega^* = \omega_{C1}^*$ , for  $E_0 \leq 0.8E_c$  plotted with respect to the average  
13  
14 shear rate,  $\gamma^* = \tau_{MW}U_0/h$ , evaluated at  $E^* = E_0/E_c = 0, 0.4, 0.8, 1.0, 2.0,$  and  $3.0$  where  
15  
16  $E_c = 1.3 \times 10^6$  (V/m) is the critical electric field for the onset of particle Quincke rotation  
17  
18 evaluated by Eq. (1). It is learned from Fig. 3 that the magnitude of the spin velocity within the  
19  
20 flow field increases as the applied electric field strength is increased with  $\gamma^*$  kept constant. On  
21  
22 the other hand, the ER fluid spin magnitude also increases as the average shear rate,  $\gamma^*$ , or the  
23  
24 applied velocity of the upper boundary,  $U_0$ , increases while the electric field strength is kept  
25  
26 constant. As the applied electric field,  $E_0$  or  $E^*$ , is gradually reduced, the ER fluid spin velocity  
27  
28 gradually reduces back to the zero electric field angular velocity of a continuum fluid parcel, *i.e.*,  
29  
30  $\omega_0^* = -\gamma^*/2$ , or half of the Couette flow vorticity, which can be readily deduced from Eq. (32)  
31  
32 by letting  $M^* \rightarrow \infty$  or  $E_0 \rightarrow 0$ . This solution is noted by the top most, gray line with  $E^* = 0$  in  
33  
34 Fig. 3.  
35  
36  
37

38 Notice that for a given field strength and shear rate, the spin velocity,  $\omega^*$  or  $\omega_x$ , is a constant  
39  
40 throughout the channel and, thus, does not depend on the spatial  $z$ -coordinate as already  
41  
42 discussed in Section 3.2 for the Couette geometry. With the spin velocity being a constant in Eq.  
43  
44 (22), the velocity field of Couette flow with internal micro-particle electrorotation is found to be  
45  
46 the same as that of Couette flow *without* particles—a result consistent with those given in  
47  
48 Shliomis [39] and Rosensweig [22]. Thus, the velocity field of Couette flow with micro-particle  
49  
50 electrorotation in the zero spin viscosity limit is simply the linear profile given by Eq. (30).

51 Figure 4 shows the effective viscosity,  $\eta^* = \eta_{eff}/\eta$ , of Couette flow with internal micro-  
52  
53 particle electrorotation as given in Eq. (38). The effective viscosity is plotted with respect to the  
54  
55 average shear rate,  $\gamma^*$ , with the electric field strength being evaluated at  $E^* = 0, 0.4, 0.8, 1.0,$   
56  
57  $2.0,$  and  $3.0$ . Again, the spin velocity solution given by Eq. (33) is employed in Eq. (38) for  
58  
59 conditions of  $E^* = E_0/E_c \geq 1$ , whereas Eq. (34) is employed in Eq. (38) for  $E^* \leq 0.8$ . It is readily  
60  
61  
62  
63  
64  
65

1  
2  
3  
4 seen that the effective viscosity decreases as the applied DC electric field strength increases.  
5  
6 However, as the magnitude of the shear rate increases, the amount of reduction in the effective  
7  
8 viscosity decreases regardless of the applied electric field strength. Since the effective viscosity  
9  
10 is normalized and non-dimensionalized by the zero electric field ER fluid viscosity,  $\eta$ , we  
11  
12 further point out that the value of  $\eta^*$  should approach one as the applied electric field goes to  
13  
14 zero, which is a result easily found by substituting  $\omega_0^* = -\gamma^*/2$  into Eq. (38). The zero electric  
15  
16 field result is indicated by the gray line in Fig. 4. It can be seen from the figure that the predicted  
17  
18 effective viscosities  $\eta^*$  approach to one when the shear rate,  $\gamma^*$ , goes large or when the applied  
19  
20 electric field strength is reduced.  
21

22 From Fig. 4, we find that zero or negative viscosities are attainable when the applied DC  
23  
24 electric field strength is strong enough. By using the terms “zero or negative viscosities,” we do  
25  
26 not mean that the true fluid viscosity is zero or negative, but that the effective or apparent  
27  
28 viscosity comes out to be zero or a negative value through performing the force balance  
29  
30 described by Eqs. (37) and (38) when the boundary shear stress,  $\tau_s$ , is maintained a constant. In  
31  
32 experimental terms, as the applied electric field strength becomes large, the “pumping” or  
33  
34 “conveyer belt” effect of the micro-particles undergoing electrorotation on the ER fluid  
35  
36 continuum becomes so significant that the ER fluid spin or rotation itself, instead of some  
37  
38 externally applied force or torque, provides the shear stress required to move the upper plate of  
39  
40 the Couette geometry. Therefore, we may observe a finite shear rate,  $\gamma^*$ , or plate velocity,  $U_0$ ,  
41  
42 while the readings on the rheometer or viscometer indicate a zero torque applied to the fluid. As  
43  
44 for negative effective viscosity conditions, the electrorotation conveyer belt is so effective that  
45  
46 the rheometer or viscometer needs to “hold back” the Couette driving plate to maintain some  
47  
48 value of applied torque or shear rate. Further discussions can be found in Lobry and Lemaire [7]  
49  
50 for the rheometric experimental considerations and in Rinaldi *et al.* [40] for experimental torque  
51  
52 measurements on ferrofluids subjected to rotating magnetic fields.

53 The effective viscosity solutions given by the present continuum model can be compared  
54  
55 with the theoretical and experimental results found in Lemaire *et al.* [12] by using the same  
56  
57 carrier liquid conductivity,  $\sigma_1 = 1.5 \times 10^{-8}$  (S/m), and other material parameters in the numerical  
58  
59 evaluations of the present continuum model. Using their material properties and parameters, the  
60  
61  
62  
63  
64  
65

1  
2  
3  
4 corresponding critical electric field for the onset of Quincke rotation is evaluated to be  $E_c \approx 0.83$   
5  
6 (kV/mm). We find that the continuum model predicted effective viscosity,  $\eta^*$ , varies in a  
7  
8 similar trend with respect to  $\gamma^*$  and/or  $E^*$  as compared with the theoretical predictions from the  
9  
10 two-phase volume averaged model (single particle dynamics based) shown in Figs. 7(a) and 7(b)  
11  
12 of Lemaire *et al.* [12]. Unlike the model based on single particle dynamics in Ref. [12] which  
13  
14 over estimates the reduction in effective viscosity, the present continuum model under estimates  
15  
16 the reduction in  $\eta^*$  at high electric field strengths, but falls closer to the experimental data shown  
17  
18 in Figs. 7(a) and 7(b) of Ref. [12] at relatively moderate electric field strengths, *i.e.*,  
19  
20  $E^* = E_0/E_c \approx 1.2$  and 2.4. This comparison between our continuum model predictions and the  
21  
22 experimental data found from Lemaire *et al.* [12] is shown in Figs. 5a and 5b for micro-particle  
23  
24 solid volume fractions of  $\phi=0.05$  and 0.1, respectively.  
25  
26  
27  
28  
29

#### 30 **4. Poiseuille Flow with Internal Micro-particle Electrorotation**

##### 31 *4.1 The Governing Equations Specific to the Poiseuille Flow Geometry*

32 **Figure 6** shows the schematic diagram of a parallel plate Poiseuille flow. Instead of an upper  
33  
34 plate moving at a constant velocity  $U_0$ , the upper and lower plates are now both fixed at zero  
35  
36 velocity, and a pressure gradient,  $\Gamma \equiv -\partial p/\partial y$ , is applied in the positive  $y$ -direction, *i.e.*,  $\Gamma > 0$ ,  
37  
38 through the channel to drive the fluid flow. Based on the similar geometries given for both  
39  
40 Couette and Poiseuille cases, we again assume that the flow is steady, incompressible, two-  
41  
42 dimensional, and fully developed so that the  $z$ -velocity component, *i.e.*,  $u_z$  in  $\bar{\mathbf{v}} = u_y \bar{\mathbf{i}}_y + u_z \bar{\mathbf{i}}_z$ , is  
43  
44 identically zero and that the applied pressure gradient,  $\Gamma$ , is a constant for a fully developed  
45  
46 flow. The applied DC electric field is further approximated to be only in the  $z$ -direction, namely,  
47  
48  $\bar{\mathbf{E}} = E_z \bar{\mathbf{i}}_z$ , with  $E_z \approx E_0$  and  $E_0$  being a constant across the channel height,  $h$ .  
49  
50  
51

52 For zero spin viscosity conditions, Eqs. (3), (4), and (20) then reduce to Eqs. (21), (23), and

$$53 \Gamma + 2\zeta \frac{d\omega_x}{dz} + \eta_e \frac{d^2 u_y}{dz^2} = 0, \quad (39)$$

54 where  $\bar{\omega} = \omega_x \bar{\mathbf{i}}_x$  for our 2D geometry. After substituting Eq. (19) into Eq. (21) and solving Eqs.  
55  
56 (21a) and (21b), we again arrive at Eqs. (24) and (25). Using Eqs. (24a) and (25) in Eq. (23), we  
57  
58  
59  
60  
61  
62  
63  
64  
65

obtain the set of governing equations for Poiseuille flow with internal micro-particle electrorotation, that is, Eqs. (39) and (27).

Since we are considering zero spin viscosities in the angular momentum equation, the spin velocity field,  $\bar{\omega} = \omega_x \bar{i}_x$ , again follows the “free-to-spin” condition at the boundaries while we apply the no-slip BC,  $\bar{v} = 0$ , at  $z=0$  and  $h$  on the velocity field,  $\bar{v} = u_y(z) \bar{i}_y$ . Yet, for a Poiseuille geometry, the spin velocity is no longer a constant throughout the flow field, *i.e.*,  $\bar{\omega} = \omega_x(z) \bar{i}_x$ , and thus a geometric condition for the spin velocity field, namely,  $\bar{\omega} \rightarrow 0$ , is needed as  $z \rightarrow h/2$  so as to satisfy the symmetry requirements imposed by the symmetric parallel plate Poiseuille flow boundaries [23]. Also, based on the stable rotation requirement on the rotating micro-particles, we require the micro-particle rotation speed to approach zero at the mid-plane of the flow channel, *i.e.*,  $\bar{\Omega} \rightarrow 0$  as  $z \rightarrow h/2$ , since the macroscopically imposed Poiseuille vorticity is positive (counter clockwise rotation) in the upper half of the flow channel, negative (clockwise rotation) in the lower half of the flow channel, and thus approaches zero at the mid-plane or center of the channel.

#### 4.2 Solutions to the Spin Velocity Profile, Linear Velocity Profile, and the Volume Flow Rate

Following a similar procedure to that of the Couette geometry case, we integrate Eq. (39) to have

$$\Gamma z + 2\zeta\omega_x + \eta_e \frac{du_y}{dz} = C_p, \quad (40)$$

where  $C_p$  is a constant. Equation (40) is then substituted into Eq. (27) so that the angular momentum equation becomes

$$\frac{\alpha^* - \tau_{MW}\omega_x}{1 + \tau_{MW}^2\omega_x^2} n\alpha_z E_0^2 + 2\zeta \left( \frac{\Gamma}{\eta_e} z + \frac{2\zeta}{\eta_e} \omega_x - \frac{C_p}{\eta_e} - 2\omega_x \right) = 0. \quad (41)$$

By applying the symmetry conditions,  $\bar{\omega} \rightarrow 0$  and  $\bar{\Omega} \rightarrow 0$  (*i.e.*,  $\omega_x \rightarrow 0$  and  $\Omega \rightarrow 0$ ) as  $z \rightarrow h/2$ , to Eq. (41) and recalling that  $\alpha^* = \alpha_y/\alpha_z = -\tau_{MW}\Omega$ , the constant  $C_p$  is determined to be  $\Gamma h/2$ , and Eq. (41) is rewritten as

$$\frac{\alpha^* - \tau_{MW}\omega_x}{1 + \tau_{MW}^2\omega_x^2} - \frac{n\alpha_z E_0^2}{2\zeta} + \frac{\Gamma h}{\eta_e} \left( \frac{z}{h} - \frac{1}{2} \right) - \frac{2\eta}{\eta_e} \omega_x = 0, \quad (42)$$

which is an algebraic, cubic equation with the  $z$ -coordinate being a spatially varying coefficient.

Using the following non-dimensionalization scheme, namely,

$$\omega^* = \tau_{MW}\omega_x, \quad z^* = \frac{z}{h}, \quad m^* = \frac{2\zeta\eta}{n\alpha_z E_0^2 \tau_{MW} \eta_e}, \quad \text{and} \quad V^* = \frac{\Gamma h \tau_{MW}}{\eta} m^*, \quad (43)$$

Eq. (42) is non-dimensionalized and the dimensionless angular momentum equation for the Poiseuille case becomes

$$\omega^{*3} - \frac{V^*}{2m^*} \left( z^* - \frac{1}{2} \right) \omega^{*2} + \left( 1 + \frac{1}{2m^*} \right) \omega^* - \frac{V^*}{2m^*} \left( z^* - \frac{1}{2} \right) - \frac{\alpha^*}{2m^*} = 0. \quad (44)$$

We solve Eq. (44) by standard symbolic calculation packages (Mathematica, Wolfram Research, Inc.) to express  $\omega^*$  in terms of  $V^*$ ,  $z^*$ , and  $m^*$ , or equivalently, to express  $\omega_x$  in terms of  $z$ ,  $\Gamma$ , and  $E_0$ . The stability, real valued, and free-to-spin conditions are then applied to select or pick out the most physically meaningful solution or combination of solutions to the spin velocity,  $\omega^*$ , from the three possible roots, *e.g.*,  $\omega_{p1}^*$ ,  $\omega_{p2}^*$ , and  $\omega_{p3}^*$ , found in solving the angular momentum equation, Eq. (44). Recall from Section 3.2 that for  $E_0 \geq E_c$ , we require the suspended micro-particles to rotate in the direction of the macroscopic flow vorticity, which in this case, is the Poiseuille flow vorticity direction. Based on this requirement and referring to the coordinate systems shown in Figs. 1 and 6, we apply the negative valued micro-particle rotation speed  $\Omega$ , *i.e.*, clockwise or pointing into the plane, in Eq. (17) to Eqs. (24) and (25) for the lower half of the channel, *i.e.*,  $0 \leq z^* < 1/2$ , and the positive valued  $\Omega$ , *i.e.*, counter clockwise or pointing out of the plane, in Eq. (17) to Eqs. (24) and (25) for the upper half of the channel, *i.e.*,  $1/2 < z^* \leq 1$ . On the other hand, for  $E_0 < E_c$ , we set  $\Omega = 0$  in Eqs. (24) and (25) and require the real valued spin velocity  $\omega^*$  to be negative in  $0 \leq z^* < 1/2$  and to be positive in  $1/2 < z^* \leq 1$ . Figure 7 shows the real valued results of the spin velocity,  $\omega^*$ , plotted with respect to the spatial coordinate,  $z^*$ , with  $\Gamma = 2 \times 10^4$  (Pa/m) at  $E^* = 1.0, 1.01, \text{ and } 1.05$  for both Figs. 7a and 7b and at  $E^* = 0.7, 0.8, 0.9, 0.95, \text{ and } 0.99$  for Fig. 7c where  $E^* = E_0/E_c$  with  $E_c = 1.3 \times 10^6$  (V/m); the dash-dash curves represent a first root,  $\omega_{p1}^*$ , the dash-dot-dash curves represent a second root,

$\omega_{p_2}^*$ , and the solid gray curves represent the last root,  $\omega_{p_3}^*$ . Although the spin velocity profiles extend across the whole channel domain,  $0 \leq z^* \leq 1$ , the solutions for  $E^* > 1$  shown in Fig. 7a are only valid for  $1/2 < z^* \leq 1$  since we have employed in Eqs. (24) and (25) the positive valued  $\Omega$  of Eq. (17) that corresponds to the positive vorticity in  $1/2 < z^* \leq 1$  to satisfy the stable micro-particle rotation requirement during the numerical evaluation of the figure. Similarly, the spin velocity profiles for  $E^* > 1$  shown in Fig. 7b are only valid for  $0 \leq z^* < 1/2$  since the negative valued particle rotation speed  $\Omega$  of Eq. (17) corresponding to the negative vorticity in  $0 \leq z^* < 1/2$  has been employed in Eqs. (24) and (25) when evaluating the solutions throughout the whole spatial domain. For spin velocity profiles shown in Fig. 7c as well as for the  $E^* = 1$  solutions shown in both Figs. 7a and 7b, we find that with  $\Omega = 0$  in Eqs. (24) and (25) (note: Eq. (17) goes to zero when  $E^* = 1$ ), the spin velocity profiles become s-shaped centered at  $z^* = 0.5$ , and become multi-valued with respect to the spatial coordinate,  $z^*$ , near the middle of the flow channel when  $\Gamma = 2 \times 10^4$  ( $Pa/m$ ) and  $E^* = 0.95 \sim 1.0$ . This is a similar non-linear behavior found in AC or traveling wave ferrofluid spin velocity profiles under zero spin viscosity,  $\eta' = 0$ , conditions as discussed in Zahn and Pioch [41, 42]. However, since multi-valued spin velocity profiles will eventually lead to linear velocity profiles that are multi-valued in space, the situation is less likely to be physical for steady, viscous, and fully developed fluid flows [41, 42]. Therefore, resolution is made by requiring  $\omega^* \rightarrow \omega_{p_3}^* = 0$  at  $z^* = 1/2$  and discarding the  $\omega_{p_1}^*$  and  $\omega_{p_3}^*$  solutions in  $0 \leq z^* < 1/2$  and the  $\omega_{p_2}^*$  and  $\omega_{p_3}^*$  solutions in  $1/2 < z^* \leq 1$ , that is, use the negative valued  $\omega^*$ , i.e.,  $\omega_{p_2}^*$ , in  $0 \leq z^* < 1/2$  and the positive  $\omega^*$ , i.e.,  $\omega_{p_1}^*$ , in  $1/2 < z^* \leq 1$ , so that the final solution is real valued, stable, symmetric, free-to-spin, and more likely physical for  $\Gamma = 2 \times 10^4$  ( $Pa/m$ ) and  $E^* = 0.95 \sim 1.0$  conditions. Finally, for the spin velocity profiles evaluated at  $\Gamma = 2 \times 10^4$  ( $Pa/m$ ) and  $E^* \leq 0.9$  as shown in Fig. 7c, only one root,  $\omega_{p_1}^*$ , is found to be valid, that is, real valued and rotation direction in the vorticity direction, throughout the spatial domain,  $0 \leq z^* \leq 1$ .

By carefully examining Figs. 7a, 7b, and 7c and applying all the above reasoning and conditions, the explicit expressions of the final solution to the spin velocity of Poiseuille flow

with internal micro-particle electrorotation is obtained for  $E_0 \geq E_c$  as: (i) in  $0.5 < z^* \leq 1$  (substitute positive valued  $\Omega$  of Eq. (17) in Eqs. (24) and (25)),

$$\omega_{P1}^* = \frac{2V^* z^* - V^*}{12m^*} + \varphi_{P1} \left[ 6\sqrt[3]{4m^*} \left( \varphi_{P2} + \sqrt{\varphi_{P2}^2 + 4\varphi_{P1}^3} \right)^{1/3} \right]^{-1} - \frac{1}{12\sqrt[3]{2m^*}} \left( \varphi_{P2} + \sqrt{\varphi_{P2}^2 + 4\varphi_{P1}^3} \right)^{1/3}, \quad (45)$$

(ii) at  $z^* = 0.5$ ,

$$\omega_{P3}^* = 0, \quad (46)$$

and (iii) in  $0 \leq z^* < 0.5$  (using negative valued  $\Omega$  of Eq. (17) in Eqs. (24) and (25)),

$$\omega_{P2}^* = \frac{2V^* z^* - V^*}{12m^*} - \varphi_{P1} (1 + i\sqrt{3}) \left[ 12\sqrt[3]{4m^*} \left( \varphi_{P2} + \sqrt{\varphi_{P2}^2 + 4\varphi_{P1}^3} \right)^{1/3} \right]^{-1} + \frac{1}{24\sqrt[3]{2m^*}} \left[ (1 - i\sqrt{3}) \left( \varphi_{P2} + \sqrt{\varphi_{P2}^2 + 4\varphi_{P1}^3} \right)^{1/3} \right], \quad (47)$$

where

$$\varphi_{P1} = 24m^* (1 + 2m^*) - (2V^* z^* - V^*)^2, \quad (48)$$

and

$$\varphi_{P2} = -72m^* V^* + 288m^{*2} V^{*2} + 2V^{*3} + 144m^* V^* z^* - 576m^{*2} V^* z^* - 12V^{*3} z^* + 24V^{*3} z^{*2} - 16V^{*3} z^{*3} - 864m^{*2} \alpha^*. \quad (49)$$

As for electric field strengths below the critical electric field, *i.e.*,  $E_0 < E_c$ , the micro-particle rotation speed,  $\Omega$ , is set to zero in Eqs. (24) and (25), and Eq. (45) is generally valid throughout  $0 \leq z^* \leq 1$  for the pressure gradients of interest with  $E_0 \leq 0.9E_c$ . For electric field strengths of  $0.95E_c \leq E_0 < E_c$ , Eqs. (45)-(47) are used with  $\Omega = 0$  in Eqs. (24) and (25) during the evaluation of the spin velocity profile. The analytic expressions given above are obtained under the ‘‘Solve’’ command using Mathematica.

Again notice that the solution or combination of solutions given to Eq. (44) need to satisfy all the above conditions and reasoning within the parametric regimes of interest since it is less likely to be physical for solutions being complex or multi-valued. The combination of solutions, Eqs. (45)-(47), presented herein is generally for the parametric range of  $E^* = E_0/E_c = 1 \sim 3$  with  $E_c = 1.3 \times 10^6$  (V/m) and  $\Gamma^* = \Gamma/\Gamma_r = 0 \sim 2$  with  $\Gamma_r = 2 \times 10^4$  (Pa/m) in  $0 \leq z^* \leq 1$ , whereas Eq. (45) is generally valid for  $E^* \leq 0.9$  and  $0 \leq \Gamma^* \leq 2$  throughout  $0 \leq z^* \leq 1$ . For other parametric



1  
2  
3  
4 regimes of particular interests, the combination of solutions and the parametric range where the  
5 solutions becomes multi-valued *may be* different from the ones discussed herein. In this case, we  
6 need to start from Eq. (44) and solve for the three roots, then simultaneously apply the stability,  
7 symmetry, real valued, and “free-to-spin” conditions to the roots to finally pick out or select the  
8 suitable and most physical combination for the desired spin velocity field just like the procedure  
9 we have shown in this section. Also notice that the jump or discontinuity made in the final spin  
10 velocity profile at  $z^* = 0.5$  is permitted self-consistently by the “free-to-spin” condition for the  
11 zero spin viscosity cases studied herein. This is an analogous situation to the “inviscid” parallel  
12 shear flow with the *velocity field* being  $\bar{v} = U\bar{i}_y$  for  $z > 0$  and  $\bar{v} = -U\bar{i}_y$  for  $z < 0$  as one of the  
13 possible base solutions to Kelvin-Helmholtz instability studies.  
14

15 We can always rewrite Eq. (44) and express the spatial coordinate,  $z^*$ , as a function of the  
16 spin velocity,  $\omega^*$ , (*i.e.*, plot  $z^*$  by varying  $\omega^*$  instead of plot  $\omega^*$  by varying  $z^*$ ) so as to avoid  
17 encountering complex valued solutions or transition of the real valued solution from one root to  
18 another as shown in Rosensweig [22] for ferrofluid Couette flows subjected to uniform magnetic  
19 fields. However, even by this method, we will still encounter the problem of multi-valued  
20 solutions and of finding the most physically likely solution that satisfies the stable micro-particle  
21 rotation requirement for the present electrorotation flows. Moreover, as will be shortly shown in  
22 the following, since the linear velocity profile,  $u^*$ , and the 2D volume flow rate,  $Q$ , solutions  
23 depend on integrations of the spin velocity profile,  $\omega^*$ , it is much more straight forward, in terms  
24 of performing the integrations with respect to  $z^*$  without obscuring the fundamental physical  
25 meanings, to express the spin velocity as a function of the spatial coordinate, *i.e.*,  $\omega^* = \omega^*(z^*)$ ,  
26 as compared to expressing the spatial coordinate as a function of the spin velocity,  $z^* = z^*(\omega^*)$ .  
27 This is why we have chosen a seemly more difficult way of tackling Eq. (44) and explained in  
28 detail about the reasoning and conditions applied during the solution process.  
29

30 After substituting the spin velocity solutions,  $\omega^*$  or  $\omega_x$ , and  $C_p = \Gamma h/2$  into Eq. (40) and  
31 also noticing that for  $E^* \geq 1$ ,  $\omega^*$  is expressed by Eqs. (45) and (47) in the respective regions of  
32  $0.5 < z^* \leq 1$  and  $0 \leq z^* < 0.5$ , we integrate Eq. (40) with respect to the spatial coordinate,  $z^*$ , to  
33 obtain the velocity field as: (i) for  $0.5 < z^* \leq 1$ ,  
34  
35  
36  
37  
38  
39  
40  
41  
42  
43  
44  
45  
46  
47  
48  
49  
50  
51  
52  
53  
54  
55  
56  
57  
58  
59  
60  
61  
62  
63  
64  
65

$$u_{UP}^*(z^*) = \frac{\eta}{\eta_e} \left[ z^*(1-z^*) + \frac{4\zeta}{\Gamma h \tau_{MW}} \int_{z^*}^1 \omega_{p1}^*(z^*) dz^* \right], \quad (50a)$$

and (ii) for  $0 \leq z^* < 0.5$ ,

$$u_{DN}^*(z^*) = \frac{\eta}{\eta_e} \left[ z^*(1-z^*) - \frac{4\zeta}{\Gamma h \tau_{MW}} \int_0^{z^*} \omega_{p2}^*(z^*) dz^* \right], \quad (50b)$$

where the velocity field, Eq. (50), is made dimensionless by dividing with  $\Gamma h^2/2\eta$  (note: use  $\eta$  not  $\eta_e$ ), i.e.,  $u^*(z^*) = 2\eta u_y(z^*)/\Gamma h^2$ ,  $\omega_{p1}^*$  and  $\omega_{p2}^*$  are respectively defined in Eqs. (45) and (47), and  $z^*$  is a dummy index in both equations. For  $E^* \leq 0.9$ , use  $\omega_{p1}^*$ , i.e., Eq. (45), in place of  $\omega_{p2}^*$ , i.e., Eq. (47), in Eq. (50b), that is, use Eq. (45) for the spin velocities throughout  $0 \leq z^* \leq 1$  in the integration of Eq. (50). From general mathematical point of views, the velocity field of the flow,  $u_y$ , needs to be continuous and smooth (continuous in  $du_y/dz$ ) throughout the channel because of finite ER fluid viscosities,  $\eta$ . However, since we have manually (with physical reasoning) made the spin velocity,  $\omega_x$ , discontinuous at the middle of the channel, the smoothness of the velocity distribution near  $z^* = 0.5$  may not exactly be preserved under the framework of zero spin viscosity limits—a cusp may arise at  $z^* = 0.5$  in the velocity profile given by Eq. (50) for certain parametric regimes of interest. This issue will be further discussed in Section 4.3.

We next calculate the two dimensional volumetric flow rate,  $Q$ , by integrating the velocity fields, i.e.,

$$Q = \int_0^h u_y(z) dz = \frac{\Gamma h^3}{2\eta} \left[ \int_0^{0.5} u_{DN}^*(z^*) dz^* + \int_{0.5}^1 u_{UP}^*(z^*) dz^* \right], \quad (51)$$

with Eq. (50a) used for  $0.5 < z^* \leq 1$  and Eq. (50b) used for  $0 \leq z^* < 0.5$ . In terms of the spin velocities, Eq. (51) is rewritten as, for  $E^* \geq 1$ ,

$$Q = \left( \frac{\Gamma h^3}{12\eta} \right) \left( \frac{\eta}{\eta_e} \right) \left\{ 1 + \frac{24\zeta}{\Gamma h \tau_{MW}} \left[ \int_{0.5}^1 \int_{z^*}^1 \omega_{p1}^*(z^*) dz^* dz^* - \int_0^{0.5} \int_0^{z^*} \omega_{p2}^*(z^*) dz^* dz^* \right] \right\}, \quad (52)$$

where  $z^*$  is the dummy index and Eqs. (45) and (47) are used in the integration ranges of  $0.5 < z^* \leq 1$  and  $0 \leq z^* < 0.5$ , respectively. Again, for  $E^* \leq 0.9$ , use  $\omega_{p1}^*$ , i.e., Eq. (45),

throughout  $0 \leq z^* \leq 1$  in the integration of Eq. (51) or (52). It is now obvious why we use  $\eta$ , zero electric field ER fluid viscosity, instead of  $\eta_e = \eta + \zeta$  in non-dimensionalizing the velocity field of Eq. (50). The intention is to utilize the ordinary Poiseuille flow solution (no electric field applied to the ER fluid) as a reference datum so that the variation and deviation in the electroration modified Poiseuille velocities and flow rates from those of the zero electric field solutions, *i.e.*,  $u_0^*(z^*) = (2\eta/\Gamma h^2)u_y(z^*) = z^*(1-z^*)$  and  $Q_0 = \Gamma h^3/12\eta$ , can be respectively compared.

Results of the spin velocity profile, (linear) velocity profile, and the volume flow rate will be respectively presented in the following subsection. The system parameters, physical constants, and material properties used in the numeric evaluations can be found in Table 2 unless otherwise specified.

#### 4.3 Results and Discussions

Before presenting the spin velocity profiles, we first normalize the Poiseuille spin velocity, Eqs. (45)-(47) by  $\Gamma h\tau_{MW}/2\eta$ , namely,  $\omega^* = \omega_{p1}^* = 2\eta\omega_{p1}^*/\Gamma h\tau_{MW}$  for  $0.5 < z^* \leq 1$ ,  $\omega^* = \omega_{p2}^* = 2\eta\omega_{p2}^*/\Gamma h\tau_{MW}$  for  $0 \leq z^* < 0.5$ , and  $\omega^* = \omega_{p3}^* = 2\eta\omega_{p3}^*/\Gamma h\tau_{MW} = 0$  for  $z^* = 0.5$ . By employing this normalization, we find that the zero electric field solution,  $\omega_0^* = \Gamma h\tau_{MW}(z^* - 0.5)/2\eta$ , becomes independent of the applied pressure gradient and only depends on the spatial position in the channel, *i.e.*,  $\omega_0^* = (z^* - 0.5)$ . The zero electric field solution then becomes a reference datum invariant of both the applied electric field strength and the driving pressure gradient and facilitates a more physically meaningful comparison among the solutions.

Illustrated in Fig. 8 are the spatial variations of the electroration assisted Poiseuille spin velocity profiles given by Eqs. (45)-(47) normalized by  $\Gamma h\tau_{MW}/2\eta$  plotted with respect to distinct strengths of the applied electric field,  $E^* = E_0/E_c$ . With the pressure gradient kept constant, *i.e.*,  $\Gamma^* = \Gamma/\Gamma_r = 1$  where  $\Gamma_r = 2 \times 10^4$  (Pa/m), the normalized spin velocity  $\omega^*$  is evaluated at  $E^* = 0, 0.4, 0.8, 1.0, 2.0, \text{ and } 3.0$  with  $E_c = 1.3 \times 10^6$  (V/m). The solid gray curve

1  
2  
3  
4  
5 shown in Fig. 8 represents the zero electric field solution,  $\omega_0^* = (z^* - 0.5)$ , or half of the  
6  
7 Poiseuille vorticity when there is no electric field and internal micro-particle electrorotation  
8  
9 effects. From the figure, the positive and negative valued spin velocities found in the respective  
10  
11 regions of  $0.5 < z^* \leq 1$  and  $0 \leq z^* < 0.5$  (with  $\omega^* = \omega_{p3}^* = 0$  at  $z^* = 0.5$ ) show that we have  
12  
13 chosen, based on the macroscopic Poiseuille vorticity directions, the combination of solutions  
14  
15 that satisfies the symmetry, real valued, and stable particle rotation conditions. The apparent  
16  
17 jump or discontinuity in the spin velocity profile at  $z^* = 0.5$  is self-consistently permitted by the  
18  
19 “free-to-spin” condition under the framework of the zero spin viscosity limit as already  
20  
21 mentioned in the previous sections.

22  
23 As can be seen in Fig. 8, the magnitude of the normalized spin velocity of Poiseuille flow  
24  
25 with internal particle electrorotation increases as the applied DC electric field strength is  
26  
27 increased. If, on the contrary, we reduce the applied electric field strength from  $E^* = 1.0, 0.8$  to  
28  
29  $0.4$ , we find that the spin velocity gradually approaches the zero electric field solution noted by  
30  
31 the gray curve in Fig. 8. Moreover, the strength of the jump or discontinuity at  $z^* = 0.5$  in the  
32  
33 normalized spin velocity field reduces and eventually smoothes out (see the smooth and  
34  
35 continuous curves for  $E^* = 0.4$  and  $0.8$ ) as the applied electric field is decreased. Note that in  
36  
37 this figure, the solutions to  $E^* = 0.4$  and  $0.8$  are fully represented by  $\omega^* = \omega_{p1}^*$ , *i.e.*, Eq. (45),  
38  
39 throughout the spatial domain,  $0 \leq z^* \leq 1$ , at  $\Gamma^* = 1$ . However, the spin velocity solutions to  
40  
41  $E^* = 1.0, 2.0$ , and  $3.0$  are represented by  $\omega^* = \omega_{p1}^*$  (Eq. (45)) for  $0.5 < z^* \leq 1$ ,  $\omega^* = \omega_{p2}^*$  (Eq.  
42  
43 (47)) for  $0 \leq z^* < 0.5$ , and zero (Eq. (46)) for  $z^* = 0.5$  at  $\Gamma^* = 1$ . The transition among the  
44  
45 different roots verifies the cubic nature of the governing equation, Eq. (44).  
46

47 After the spin velocity field is found, the (linear) velocity field is easily obtained by  
48  
49 integrating Eq. (50). The results of the velocity field,  $u^*$  (or  $u_y$ ), are plotted with respect to the  
50  
51 spatial coordinate  $z^*$  in Fig. 9 for  $\Gamma^* = 1$  with  $E^* = 0, 0.4, 0.8, 1.0, 2.0$ , and  $3.0$ . The gray solid  
52  
53 curve represents the zero electric field solution,  $u_0^* = z^*(1 - z^*)$ , *i.e.*, the velocity field of ordinary  
54  
55 Poiseuille flow without internal micro-particle electrorotation. Recall that the velocity field was  
56  
57 already normalized by  $\Gamma h^2 / 2\eta$  in the non-dimensional definition of Eq. (50); hence, there is no  
58  
59 more need to define a normalized velocity field as in the case of the spin velocity.  
60  
61  
62  
63  
64  
65

Based upon the above convention, we find in Fig. 9 that with  $\Gamma^* = 1$  kept constant, the flow velocity is considerably enhanced and the cusp in the velocity profile at  $z^* = 0.5$  is sharpened as the strength of the applied DC electric field is increased. If we reduce the strength of the electric field while the pressure gradient is maintained constant, the cusp at  $z^* = 0.5$  becomes blunt and the electroration enhanced velocity profile gradually reduces and converges back to the  $E^* = 0$  solution, *i.e.*, the parabolic Poiseuille flow velocity field without internal particle electroration as noted by the solid gray curve in the figure. The  $E^* = 0.4$  and 0.8 velocity fields shown are evaluated by substituting Eq. (45), *i.e.*,  $\omega_{p1}^*$ , into the integrals of both Eqs. (50a) and (50b) with  $\Omega = 0$  in Eqs. (24) and (25) since in this parametric regime,  $\omega_{p1}^*$  assumes a real value and is valid throughout the spatial domain of  $0 \leq z^* \leq 1$ . As for  $E^* = 1.0, 2.0,$  and  $3.0$ , Eq. (45) is employed in the integral of Eq. (50a) whereas Eq. (47) is used in Eq. (50b). The cusped velocity profiles shown in Fig. 9 are consistent with those obtained from combined single particle dynamics and two-phase effective medium modeling [9] and are interestingly similar to the velocity profiles of a power law fluid in circular pipe Poiseuille flow geometries for large power indices [43] though, of course, the electroration and power law fluid flows work respectively on different principles.

Finally, using the physical parameters and material properties given in Table 2, the two dimensional volume flow rate of Poiseuille flow with internal micro-particle electroration,  $Q$  ( $m^2/s$ ), is plotted with respect to the driving pressure gradient,  $\Gamma^* = \Gamma/\Gamma_r$  with  $\Gamma_r = 2 \times 10^4$  ( $Pa/m$ ), at distinct values of the applied DC electric field strength,  $E^* = E_0/E_c$  with  $E_c = 1.3 \times 10^6$  ( $V/m$ ). The results are shown in Fig. 10 for  $E^* = 0, 0.4, 0.8, 1.0, 2.0,$  and  $3.0$  with the solid gray curve noted by  $E^* = 0$  corresponding to the two dimensional volume flow rate of Poiseuille flow without internal micro-particle electroration, *i.e.*,  $Q_0 = \Gamma h^3/12\eta$ .

From Fig. 10, we find that the volume flow rate increases as the applied DC electric field strength is increased while the driving pressure gradient is kept constant. On the other hand, the electroration enhanced volume flow rate gradually reduces back to the zero electric field solution,  $Q_0 = \Gamma h^3/12\eta$ , as the applied electric field is reduced. These results are consistent with our previous examination of the velocity fields shown in Fig. 9 and agree with the experimental

1 observations reported in Ref. [10]. Note that the flow rate solutions evaluated at  $E^* = 1.0, 2.0,$   
 2 and 3.0 suggest non-zero volume flow rates at zero driving pressure gradients when the flow is  
 3 subjected to an applied electric field strength greater than or equal to the critical electric field for  
 4 the onset of Quincke rotation. This result is particularly due to the fact that we have used the  
 5 combination of solutions to the spin velocity, Eqs. (45)-(47), that satisfies the symmetry, real  
 6 valued, stable micro-particle rotation, and free-to-spin conditions in the modeling and evaluation  
 7 of the volume flow rate,  $Q$ , under zero spin viscosity conditions, *i.e.*,  $\eta' = 0$ . Nonetheless, we  
 8 need to point out that unless there is some initial flow ( $\Gamma^* \neq 0$ ) applied to give the suspended  
 9 micro-particles a favorable direction for electrorotation, the direction for Quincke rotation is  
 10 merely a matter of chance with the particle rotation axis either pointing into or out of the planes  
 11 defined by the electric field under zero flow or equivalently zero driving pressure gradient  
 12 conditions. Up to this point, no experimental evidence has observed a negative ER effect with  
 13 zero initial flow when an electric field strength,  $E_0 \geq E_c$ , is applied [7]—both initial vorticity and  
 14 micro-particle Quincke rotation are needed for the present negative ER effect. The finite jump of  
 15 volume flow rate at zero driving pressure gradients diminishes and eventually becomes zero, *i.e.*,  
 16 zero flow rate at zero pressure gradient, as we reduce the applied electric field strength from  
 17  $E^* = 1.0, 0.8,$  to 0.4 as can be found in the figure. Again, for the  $E^* \leq 0.9$  solutions, *i.e.*,  $E^* = 0.4$   
 18 and 0.8, shown in Fig. 10, we have used  $\omega_{p1}^*$ , Eq. (45), throughout the spatial domain,  $0 \leq z^* \leq 1$ .

19 Summing up the findings from examining Figs. 8-10, it is found that, in general, the  
 20 magnitude of the normalized spin velocity, the normalized flow velocity, and the 2D volume  
 21 flow rate is increased as the applied electric field,  $E^*$ , is increased with the driving pressure  
 22 gradient,  $\Gamma^*$ , kept constant. Moreover, increasing the applied electric field gives rise to a more  
 23 severe jump or discontinuity at  $z^* = 0.5$  in the normalized spin velocity profile, sharpens the  
 24 cusp structure at  $z^* = 0.5$  in the (normalized) velocity profile, and results in a finite value of  
 25 volume flow rate at zero pressure gradients. Contrarily, reducing the strength of the electric field  
 26 smoothes out the cusp in the velocity profile and reduces the severity of the discontinuity at  
 27  $z^* = 0.5$  in the spin velocity field while the pressure gradient is kept constant. The (normalized)  
 28 velocity and spin velocity profiles as well as the 2D volume flow rate gradually reduce back to  
 29 the zero electric field solutions as the applied electric field strength is reduced.

1  
2  
3  
4 Lastly, as shown in Fig. 11, the theoretical predictions of the 2D Poiseuille volume flow rate  
5 from the present continuum mechanical model are compared with the experimental data found  
6 from Figs. 5 and 6 of Lemaire *et al.* [10] by using the same material and physical parameters,  
7 *e.g.*, channel height of  $h = 750$  ( $\mu m$ ) and electric field strengths of  $E_0 = 2.7$  and  $3.3$  ( $kV/mm$ ),  
8 employed therein for micro-particle solid volume fractions of  $\phi = 0.05$  (Fig. 11a) and  $0.1$  (Fig.  
9 11b). The corresponding critical electric field for the onset of micro-particle Quincke rotation is  
10 evaluated as  $E_c = 1.3 \times 10^6$  ( $V/m$ ) by substituting the material properties given in Ref. [10] into  
11 Eq. (1). It can be found from Fig. 11 that the theoretical Poiseuille volume flow rate results  
12 obtained from the present continuum analysis are in good agreement with the experimental data  
13 found from Figs. 5 and 6 of Ref. [10] despite the slight over estimation in the volume flow rate  
14 as compared to the experimental data from Ref. [10]. The theoretical predictions from both the  
15 present continuum model and the previous single particle dynamics based model give similar  
16 variations of the 2D volume flow rate with respect to the applied electric field strength and  
17 pressure gradient—the volume flow rate increases as the applied electric field increases.  
18  
19  
20  
21  
22  
23  
24  
25  
26  
27  
28  
29  
30

31 As a general conclusion of the results presented in this article, we find that, in the zero spin  
32 viscosity limit, the full continuum governing equations (from anti-symmetric/couple stress  
33 theories) employed in this article reduce to a “particulate limit” and predict similar trends of  
34 variations of the effective viscosities for Couette flow and of the two dimensional volume flow  
35 rates for Poiseuille flow as compared to the theoretical predictions from the two-phase volume  
36 averaged effective medium model (single particle dynamics based) found in the literature [7-12,  
37 19] for describing the internal micro-particle electrorotation modified flow phenomena.  
38  
39  
40  
41  
42  
43  
44  
45  
46  
47

## 48 5. Concluding Remarks

49 Two dimensional Couette and Poiseuille flows with internal, spontaneous micro-particle  
50 electrorotation, or Quincke rotation, are modeled and analyzed through a fully continuum  
51 mechanical formulation in this article. By combining the theories of particle electromechanics  
52 and continuum anti-symmetric/couple stresses, general governing equations are given to describe  
53 the physical aspects of polarization relaxation, mass conservation, momentum conservation, and  
54 angular momentum conservation involved in this novel negative electrorheological phenomena.  
55 With the assumptions of steady, incompressible, fully developed, and two dimensional flows, the  
56  
57  
58  
59  
60  
61  
62  
63  
64  
65

1  
2  
3  
4 general governing equations are respectively reduced to two algebraic, cubic equations of the ER  
5 fluid spin velocity,  $\omega^*$ , for the Couette and Poiseuille flow geometries in the limit of a zero spin  
6 viscosity in the angular momentum equation. Stability, symmetry, and “free-to-spin” conditions  
7 are then applied to the cubic spin velocity equations to pick out or select the real valued solution  
8 or combination of solutions consistent with the physical assumptions and phenomena of interest.  
9 Expressions for the effective viscosity,  $\eta^*$ , of Couette flow as well as the linear velocity field,  
10  $u^*$ , and the 2D volume flow rate,  $Q$ , of Poiseuille flow can be further derived in terms of the  
11 applied electric field,  $E^*$ , shear rate,  $\gamma^*$ , driving pressure gradient,  $\Gamma^*$ , or spatial coordinate,  $z^*$ ,  
12 by respectively substituting the most physically suitable and meaningful solution or combination  
13 of solutions to the spin velocity,  $\omega^*$ , into the linear momentum equation with the no-slip  
14 boundary conditions on the velocity field applied at the spatial boundaries. Modeling results are  
15 summarized in the following:

- 16  
17  
18  
19  
20  
21  
22  
23  
24  
25  
26  
27  
28 (i) With internal particle electrorotation, the spin velocity,  $\omega^*$ , increases as either the applied  
29 electric field strength,  $E^*$ , or the shear rate,  $\gamma^*$ , is increased for Couette flow. Contrarily, the  
30 spin velocity reduces back to the zero electric field solution ( $E^*=0$ , no particle  
31 electrorotation), *i.e.*,  $\omega_0^* = -\gamma^*/2$ , or half of the Couette flow vorticity, as the applied electric  
32 field strength is decreased. In the limit of zero spin viscosity, the linear Couette velocity  
33 profile,  $u_y(z) = U_0 z/h$ , remains invariant regardless of the applied electric field strength.  
34  
35  
36  
37  
38  
39  
40 (ii) The effective viscosity,  $\eta^*$ , is found to decrease as the applied DC electric field strength  
41 increases for Couette flow with internal particle electrorotation. However, as the driving  
42 shear rate becomes large, the amount of reduction in the effective viscosity is reduced  
43 regardless of the applied electric field strength. For a decreasing electric field strength, the  
44 effective viscosity goes back to the zero electric field solution,  $\eta^* = 1$ , *i.e.*, the zero field  
45 viscosity of the ER fluid (particle-liquid mixture),  $\eta$ .  
46  
47  
48  
49  
50  
51  
52 (iii) With a constant driving pressure gradient,  $\Gamma^*$ , the magnitude of the normalized Poiseuille  
53 spin velocity,  $\omega^*$ , as well as the jump or discontinuity in the spin velocity profile increases as  
54 the applied electric field,  $E^*$ , increases whereas the spin velocity reduces back to the zero  
55  
56  
57  
58  
59  
60  
61  
62  
63  
64  
65



1  
2  
3  
4  
5 field solution,  $\omega_0^* = (z^* - 0.5)$ , and the discontinuity in the spin velocity profile diminishes as  
6  
7  $E^*$  is reduced.

8  
9 (iv) With a constant driving pressure gradient,  $\Gamma^*$ , the magnitude of the dimensionless  
10 (normalized) Poiseuille linear velocity,  $u^*$ , as well as the sharpness of the cusp in the  
11 velocity profile increases as the applied electric field,  $E^*$ , increases. On the contrary, the  
12 velocity profile reduces back to the zero field solution,  $u_0^* = z^*(1 - z^*)$ , and the cusp in the  
13 velocity profile becomes blunt as  $E^*$  is reduced.

14  
15 (v) The two dimensional Poiseuille volume flow rate,  $Q$ , increases as the applied DC electric  
16 field strength increases whereas the electrorotation enhanced flow rate solution reduces back  
17 to the zero electric field solution,  $Q_0 = \Gamma h^3 / 12\eta$ , as the applied electric field is decreased. At  
18 zero driving pressure gradients, the electrorotation enhanced volume flow rate assumes some  
19 finite value because of the fact that we have employed the spin velocity solution that satisfies  
20 the symmetry, real valued, stable micro-particle rotation, and free-to-spin conditions in the  
21 evaluation of  $Q$  under zero spin viscosity conditions.

22  
23 (vi) Comparing the results of the Couette effective viscosity and the Poiseuille volume flow rate  
24 obtained herein with those found in current literature, we find that both the present  
25 continuum and the previous two-phase volume averaged (single particle dynamics based)  
26 models qualitatively predict the same trends of variation for the effective viscosity with  
27 respect to the electric field strength and average shear rate, and for the volume flow rate with  
28 respect to the field strength and driving pressure gradient. The similarities found between the  
29 two modeling approaches suggest that the fully continuum mechanical modeling field  
30 equations presented in this article reduces to a “particulate limit” when the spin viscosity in  
31 the continuum angular momentum equation equals to zero, *i.e.*, couple stress free conditions.  
32 Note however that the theoretical predictions of the Couette effective viscosity and Poiseuille  
33 volume flow rate obtained from the present continuum mechanical treatment are in good  
34 agreement with the experimental measurements as reported in current literature.

35  
36 Future work includes a more advanced modeling of the polarization relaxation processes in  
37 the electrorheological fluid flow, the investigation of finite spin viscosity effects on the angular  
38  
39  
40  
41  
42  
43  
44  
45  
46  
47  
48  
49  
50  
51  
52  
53  
54  
55  
56  
57  
58  
59  
60  
61  
62  
63  
64  
65

1  
2  
3  
4 momentum balances within the flow field, and the search of possible practical applications for  
5 such novel negative electrorheological phenomenon.  
6  
7  
8  
9

### 10 11 **Acknowledgements**

12  
13 H.-F. Huang is financially supported by the National Science Council (Taipei, Taiwan) through  
14 the Taiwan Merit Scholarships under grant no. TMS-094-2-A-029. This work was supported in  
15 part by the United States-Israel Binational Science Foundation (BSF) through grant no. 2004081.  
16  
17 The authors would like to thank Prof. Mark I. Shliomis of the Department of Mechanical  
18 Engineering at the Ben-Gurion University of the Negev in Israel for fruitful and insightful  
19 discussions.  
20  
21  
22  
23  
24  
25  
26  
27  
28  
29  
30  
31  
32  
33  
34  
35  
36  
37  
38  
39  
40  
41  
42  
43  
44  
45  
46  
47  
48  
49  
50  
51  
52  
53  
54  
55  
56  
57  
58  
59  
60  
61  
62  
63  
64  
65

## References

- [1] W.M. Winslow, Induced fibrillation of suspensions, *J. Appl. Phys.* 20 (1949) 1137-1140.
- [2] T.C. Halsey, Electrorheological fluids, *Science* 258 (1992) 761-766.
- [3] D.J. Klingenberg, C.F. Zukoski IV, Studies of the steady-shear behavior of electro-rheological suspensions, *Langmuir* 6 (1990) 15-24.
- [4] J.N. Foulc, P. Atten, N. Felici, Macroscopic model of interaction between particles in an electrorheological fluid, *J. Electrostat.* 33 (1994) 103-112.
- [5] C. Boissy, P. Atten, J.N. Foulc, On a negative electrorheological effect, *J. Electrostat.* 35 (1995) 13-20.
- [6] C.W. Wu, H. Conrad, Negative electrorheological effect and electrical properties of a Teflon/silicone oil suspension, *J. Rheol.* 41 (1997) 267-281.
- [7] L. Lobry, E. Lemaire, Viscosity decrease induced by a DC electric field in a suspension, *J. Electrostat.* 47 (1999) 61-69.
- [8] A. Cebers, E. Lemaire, L. Lobry, Internal rotations in dielectric suspensions, *Magnetohydrodyn.* 36 (2000) 347-364.
- [9] A. Cebers, E. Lemaire, L. Lobry, Flow modification induced by Quincke rotation in a capillary, *Int. J. Mod. Phys. B* 16 (2002) 2063-2069.
- [10] E. Lemaire, L. Lobry, N. Pannacci, Flow rate increased by electrorotation in a capillary, *J. Electrostat.* 64 (2006) 586-590.
- [11] N. Pannacci, E. Lemaire, L. Lobry, Rheology and structure of a suspension of particles subjected to Quincke rotation, *Rheol. Acta* 46 (2007) 899-904.
- [12] E. Lemaire, L. Lobry, N. Pannacci, F. Peters, Viscosity of an electro-rheological suspension with internal rotations, *J. Rheol.* 52 (2008) 769-783.
- [13] G. Quincke, Ueber rotationen im constanten electrischen felde, *Ann. Phys. Chem.* 59 (1896) 417-486.
- [14] J.R. Melcher, G.I. Taylor, Electrohydrodynamics: a review of the role of interfacial shear stresses, *Annu. Rev. Fluid Mech.* 1 (1969) 111-146.
- [15] J.R. Melcher, Electric fields and moving media, *IEEE Trans. Educ.* E-17 (1974) 100-110.
- [16] J.R. Melcher, *Continuum Electromechanics*, The MIT Press, Cambridge, MA, 1981.
- [17] T.B. Jones, Quincke rotation of spheres, *IEEE Trans. Ind. Appl.* IA-20 (1984) 845-849.

- 1  
2  
3  
4 [18] T.B. Jones, *Electromechanics of Particles*, Cambridge University Press, New York, NY,  
5 1995.  
6  
7 [19] H. Brenner, *Rheology of two-phase systems*, *Annu. Rev. Fluid Mech.* 2 (1970) 137-176.  
8  
9 [20] R. Moskowitz, R.E. Rosensweig, *Nonmechanical torque-driven flow of a ferromagnetic*  
10 *fluid by an electromagnetic field*, *Appl. Phys. Lett.* 11 (1967) 301-303.  
11  
12 [21] R.E. Rosensweig, J. Popplewell, R.J. Johnston, *Magnetic fluid motion in rotating field*, *J.*  
13 *Magn. Magn. Mater.* 85 (1990) 171-180.  
14  
15 [22] R.E. Rosensweig, *Ferrohydrodynamics*, reprint ed., Dover Publications, Mineola, NY, 1997.  
16  
17 [23] X. He, *Ferrohydrodynamic flows in uniform and non-uniform rotating magnetic fields*,  
18 *Ph.D. Dissertation*, Department of Electrical Engineering and Computer Science,  
19 Massachusetts Institute of Technology, Cambridge, MA, 2006.  
20  
21 [24] S.M. Elborai, *Ferrofluid surface and volume flows in uniform rotating magnetic fields*,  
22 *Ph.D. Dissertation*, Department of Electrical Engineering and Computer Science,  
23 Massachusetts Institute of Technology, Cambridge, MA, 2006.  
24  
25 [25] A. Chaves, C. Rinaldi, S. Elborai, X. He, M. Zahn, *Bulk flow in ferrofluids in a uniform*  
26 *rotating magnetic field*, *Phys. Rev. Lett.* 96 (2006) 194501.  
27  
28 [26] A. Chaves, F. Gutman, C. Rinaldi, *Torque and bulk flow of ferrofluid in an annular gap*  
29 *subjected to a rotating magnetic field*, *Trans. ASME-J. Fluid. Eng.* 129 (2007) 412-422.  
30  
31 [27] A. Chaves, M. Zahn, C. Rinaldi, *Spin-up flow of ferrofluids: asymptotic theory and*  
32 *experimental measurements*, *Phys. Fluid.* 20 (2008) 053102.  
33  
34 [28] J.S. Dahler, L.E. Scriven, *Angular momentum of continua*, *Nat.* 192 (1961) 36-37.  
35  
36 [29] J.S. Dahler, L.E. Scriven, *Theory of structured continua. I. General consideration of angular*  
37 *momentum and polarization*, *Proc. Roy. Soc. A* 275 (1963) 504-527.  
38  
39 [30] D.W. Condiff, J.S. Dahler, *Fluid mechanical aspects of anti-symmetric stress*, *Phys. Fluid.* 7  
40 (1964) 842-854.  
41  
42 [31] A.C. Eringen, *Theory of micropolar fluids*, *J. Math. Mech.* 16 (1966) 1-16.  
43  
44 [32] K.R. Schumacher, I. Sellien, G.S. Knoke, T. Cader, B.A. Finlayson, *Experiment and*  
45 *simulation of laminar and turbulent ferrofluid pipe flow in an oscillating magnetic field*,  
46 *Phys. Rev. E* 67 (2003) 026308.  
47  
48 [33] S. Feng, A.L. Graham, J.R. Abbott, H. Brenner, *Anti-symmetric stresses in suspensions:*  
49 *vortex viscosity and energy dissipation*, *J. Fluid Mech.* 563 (2006) 97-122.  
50  
51  
52  
53  
54  
55  
56  
57  
58  
59  
60  
61  
62  
63  
64  
65

- 1  
2  
3  
4 [34] H.A. Haus, J.R. Melcher, *Electromagnetic Fields and Energy*, Prentice-Hall, Englewood  
5 Cliffs, NJ, 1989.  
6  
7 [35] A. O. Cebers, Internal rotation in the hydrodynamics of weakly conducting dielectric  
8 suspensions, *Mekhanika Zhidkosti i Gaza* 2 (1980) 86-93. (see also *Fluid Dyn.* 15 (1980)  
9 245-251)  
10  
11 [36] J.J. Xiao, J.P. Huang, K.W. Yu, Dynamic polarizability of rotating particles in  
12 electrorheological fluids, *J. Phys. Chem. B* 112 (2008) 6767-6771.  
13  
14 [37] M.I. Shliomis, Certain gyromagnetic effect in a liquid paramagnet, *Sov. Phys. JEPT* 39  
15 (1974) 701-704.  
16  
17 [38] M.I. Shliomis, Nonlinear effects in suspension of ferromagnetic particles under action of a  
18 rotating magnetic field, *Sov. Phys. Dokl.* 19 (1975) 686-687.  
19  
20 [39] M.I. Shliomis, Effective viscosity of magnetic suspensions, *Sov. Phys. JETP* 34 (1972)  
21 1291-1294.  
22  
23 [40] C. Rinaldi, F. Gutman, X. He, A.D. Rosenthal, M. Zahn, Torque measurements on  
24 ferrofluid cylinders in rotating magnetic fields, *J. Magn. Magn. Mater.* 289 (2005) 307-310.  
25  
26 [41] M. Zahn, L.L. Pioch, Magnetizable fluid behavior with effective positive, zero, or negative  
27 dynamic viscosity, *Indian J. Eng. Mater. Sci.* 5 (1998) 400-410.  
28  
29 [42] M. Zahn, L.L. Pioch, Ferrofluid flows in AC and traveling wave magnetic fields with  
30 effective positive, zero or negative dynamic viscosity, *J. Magn. Magn. Mater.* 201 (1999)  
31 144-148.  
32  
33 [43] R.P. Chhabra, J.F. Richardson, *Non-newtonian Flow in the Process Industries:  
34 Fundamentals and Engineering Applications*, Butterworth-Heinemann, Boston, MA, 1999.  
35  
36  
37  
38  
39  
40  
41  
42  
43  
44  
45  
46  
47  
48  
49  
50  
51  
52  
53  
54  
55  
56  
57  
58  
59  
60  
61  
62  
63  
64  
65

## Table Captions

Table 1. Summary of physical analogy between the electrorotation and ferrofluid spin-up flows.

Table 2. System parameters, physical constants, and material properties used in the numerical evaluations [7-12].

## Figure Captions

Figure 1. The schematic diagram for the problem of solving the EQS fields within and outside a spherical particle of radius  $R$  (with conductivity of  $\sigma_2$  and permittivity of  $\varepsilon_2$ ) suspended in a liquid medium (with  $\sigma_1, \varepsilon_1$ ) rotating at constant angular velocity  $\overline{\Omega} = \Omega \overline{i}_x$  subjected to a uniform DC electric field,  $\overline{E}^\dagger = E_0 \overline{i}_z$ .

Figure 2. The schematic diagram illustrating the geometry, dimensions, and physical parameters for Couette flow with internal micro-particle electrorotation.

Figure 3. The dimensionless Couette spin velocity,  $\omega^*$ , plotted with respect to the average shear rate,  $\gamma^*$ , evaluated at  $E^* = 0, 0.4, 0.8, 1.0, 2.0,$  and  $3.0$ . For  $E^* \geq 1.0$ , the spin velocity is given by Eq. (33), *i.e.*,  $\omega^* = \omega_{C2}^*$  (negative valued  $\Omega$  from Eq. (17) used in Eqs. (24) and (25)), whereas for the cases of  $E^* \leq 0.8$ ,  $\omega^*$  is given by Eq. (34),  $\omega^* = \omega_{C1}^*$ , with the micro-particle rotation speed,  $\Omega$ , set to zero in Eqs. (24) and (25). The gray line denotes the zero electric field spin velocity, namely, half of the fluid vorticity,  $\omega_0^* = -\gamma^*/2$ .

Figure 4. The effective viscosity,  $\eta^*$ , found for Couette flow plotted with respect to the average shear rate,  $\gamma^*$ , evaluated at  $E^* = 0, 0.4, 0.8, 1.0, 2.0,$  and  $3.0$ . For  $E^* \geq 1.0$ , the spin velocity given by Eq. (33), *i.e.*,  $\omega^* = \omega_{C2}^*$ , is used in the evaluation of Eq. (38), whereas for  $E^* \leq 0.8$ ,  $\omega^* = \omega_{C1}^*$  given by Eq. (34) is employed in Eq. (38). The gray line denotes the zero electric field value of the effective viscosity, *i.e.*,  $\eta^* = \eta_{eff}/\eta = 1$ , with the value of  $\eta$  given in Table 2.

Figure 5. The present continuum modeling results of effective viscosity,  $\eta^*$ , versus average shear rate,  $\gamma^*$ , are compared with the experimental data found from Lemaire *et al.* [12] at electric field strengths of  $E_0 = 1$  (diamond), 2 (triangle), and 3 (box) ( $kV/mm$ ) for micro-

particle solid volume fractions of  $\phi=0.05$  (Fig. 5a) and 0.1 (Fig. 5b). Using the material properties from Ref. [12], the corresponding critical electric field for Quincke rotation is evaluated to be  $E_c \approx 0.83$  (kV/mm).

Figure 6. The schematic diagram illustrating the geometry, dimensions, and physical parameters for Poiseuille flow with internal micro-particle electrorotation.

Figure 7. The three roots,  $\omega_{p1}^*$ ,  $\omega_{p2}^*$ , and  $\omega_{p3}^*$ , of the dimensionless Poiseuille spin velocity,  $\omega^*$ , to the angular momentum equation, Eq. (44). The spin velocity profiles are plotted with respect to the spatial coordinate,  $z^*$ , at  $\Gamma = 2 \times 10^4$  (Pa/m) and  $E^* = E_0/E_c = 1.0, 1.01, \text{ and } 1.05$  for both Figs. 7a and 7b, and  $E^* = 0.7, 0.8, 0.9, 0.95, \text{ and } 0.99$  for Fig. 7c with  $E_c = 1.3 \times 10^6$  (V/m). The dash-dash curves denote  $\omega_{p1}^*$ , the dash-dot-dash curves denote  $\omega_{p2}^*$ , and the solid gray curves denote  $\omega_{p3}^*$ . In Fig. 7a, we have substituted the positive valued particle rotation speed,  $\Omega$ , of Eq. (17) into Eqs. (24) and (25) in evaluating the spin velocity profiles. Therefore, the profiles shown in Fig. 7a are only valid within the spatial region of  $0.5 < z^* \leq 1$ . Similarly, a negative valued  $\Omega$  from Eq. (17) has been used in Eqs. (24) and (25), and thus, the spin velocity profiles shown in Fig. 7b are only valid within  $0 \leq z^* < 0.5$ . As for Fig. 7c, the particle rotation speed is set to zero,  $\Omega = 0$ , in Eqs. (24) and (25). It can be seen that the spin velocity profiles evaluated at electric fields strengths of  $E^* = 0.95 \sim 1$  become multi-valued in space near the middle of the flow channel (note that  $\Omega$  goes to zero for  $E^* = 1$  in Eq. (17)).

Figure 8. The normalized Poiseuille spin velocity profile,  $\omega^*$ , plotted with respect to the spatial coordinate,  $z^*$ , evaluated at  $E^* = 0, 0.4, 0.8, 1.0, 2.0, \text{ and } 3.0$ , with  $\Gamma^* = 1$ . The gray curve denotes the zero electric field value for the spin velocity, *i.e.*, the vorticity of ordinary Poiseuille flow. Note that Eqs. (45) and (47), with the proper selection of the micro-particle rotation speeds in Eq. (17), are used in the evaluation of the spin velocity for  $E^* \geq 1$ , whereas for  $E^* \leq 0.9$ , Eq. (45) (with  $\Omega = 0$  in Eqs. (24) and (25)) is used throughout the spatial domain of interest.

Figure 9. The normalized linear velocity profile,  $u^*$ , of Poiseuille flow with internal micro-particle electrorotation plotted with respect to the spatial coordinate,  $z^*$ , evaluated at  $E^* = 0, 0.4, 0.8, 1.0, 2.0, \text{ and } 3.0$ , with  $\Gamma^* = 1$ . The gray curve denotes the zero electric field velocity

1  
2  
3  
4 profile, which is the original Poiseuille parabolic profile. Equations (45) (use positive  $\Omega$  from  
5 Eq. (17) in Eqs. (24) and (25)) and (47) (use negative  $\Omega$  from Eq. (17) in Eqs. (24) and (25))  
6 are respectively employed in the integrals of Eqs. (50a) and (50b) for  $E^* \geq 1$ . The evaluation  
7 of  $u^*$  for  $E^* \leq 0.9$  is done by employing Eq. (45) in both Eqs. (50a) and (50b) with  $\Omega = 0$  in  
8 Eqs. (24) and (25).  
9

10  
11  
12  
13  
14 Figure 10. The two dimensional Poiseuille volume flow rate,  $Q$  ( $m^2/s$ ), plotted with respect to  
15 the applied pressure gradient,  $\Gamma^*$ , evaluated at  $E^* = 0, 0.4, 0.8, 1.0, 2.0,$  and  $3.0$ . The gray  
16 curve represents the zero electric field volume flow rate given by  $Q_0 = \Gamma h^3 / 12\eta$ .  
17  
18

19  
20  
21 Figure 11. The theoretical predictions of the volume flow rate,  $Q$  ( $m^2/s$ ), versus pressure  
22 gradient,  $\Gamma$  ( $Pa/m$ ), obtained by the present continuum treatment are compared with the  
23 experimental measurements given in Lemaire *et al.* [10] for micro-particle solid volume  
24 fractions of  $\phi = 0.05$  (Fig. 11a) and  $0.1$  (Fig. 11b) at electric field strengths of  $E_0 = 2.7$   
25 (triangle) and  $3.3$  (box) ( $kV/mm$ ). Using the material properties given in Ref. [10], the critical  
26 electric field for the onset of particle Quincke rotation is evaluated to be  $E_c = 1.3$  ( $kV/mm$ ).  
27  
28  
29  
30  
31  
32  
33  
34  
35  
36  
37  
38  
39  
40  
41  
42  
43  
44  
45  
46  
47  
48  
49  
50  
51  
52  
53  
54  
55  
56  
57  
58  
59  
60  
61  
62  
63  
64  
65



## Tables

Table 1.

	Electrorotation flow	Ferrofluid spin-up flow
Particles	Insulating dielectric micro-particles	Magnetic nanoparticles
Microscopic dipole	Maxwell-Wagner induced dipole	Permanent magnetic dipole
Macroscopic polarization	Retarding polarization $\bar{P}$	Magnetization $\bar{M}$
Applied field	DC electric field $\bar{E}$ (with vorticity)	Rotating magnetic field $\bar{H}$
Body torque density	$\bar{P} \times \bar{E}$	$\mu_0 \bar{M} \times \bar{H}$

Table 2.

Item	Description	Value	Units
$d$	Micro-particle diameter	$8.00 \times 10^{-5}$	$m$
$E_c$	Critical electric field strength	$1.30 \times 10^6$	$V/m$
$h$	Channel height	$1.00 \times 10^{-3}$	$m$
$n$	Particle number density	$3.73 \times 10^{11}$	$1/m^3$
$\varepsilon_1$	Permittivity of carrier liquid	$3.27 \times 10^{-11}$	$C^2/Nm^2$
$\varepsilon_2$	Permittivity of particles	$2.30 \times 10^{-11}$	$C^2/Nm^2$
$\phi$	Solid volume fraction of the particles	$1.00 \times 10^{-1}$	----
$\eta_0$	Carrier liquid viscosity (no particles)	$1.20 \times 10^{-2}$	$Pa \cdot s$
$\eta'$	Spin viscosity	0	$N \cdot s$
$\eta$	Zero field fluid viscosity (w/ particles)	$1.53 \times 10^{-2}$	$Pa \cdot s$
$\eta_e$	$\eta_e = \eta + \zeta$	$1.76 \times 10^{-2}$	$Pa \cdot s$
$\sigma_1$	Conductivity of the carrier liquid	$4.00 \times 10^{-8}$	$S/m$
$\sigma_2$	Conductivity of the particles	$1.00 \times 10^{-14}$	$S/m$
$\tau_{MW}$	Maxwell-Wagner relaxation time	$1.11 \times 10^{-3}$	$s$
$\zeta$	Vortex viscosity	$1.80 \times 10^{-3}$	$Pa \cdot s$

## Tables

Table 1.

	Electrorotation flow	Ferrofluid spin-up flow
Particles	Insulating dielectric micro-particles	Magnetic nanoparticles
Microscopic dipole	Maxwell-Wagner induced dipole	Permanent magnetic dipole
Macroscopic polarization	Retarding polarization $\bar{P}$	Magnetization $\bar{M}$
Applied field	DC electric field $\bar{E}$ (with vorticity)	Rotating magnetic field $\bar{H}$
Body torque density	$\bar{P} \times \bar{E}$	$\mu_0 \bar{M} \times \bar{H}$

Table 2.

Item	Description	Value	Units
$d$	Micro-particle diameter	$8.00 \times 10^{-5}$	$m$
$E_c$	Critical electric field strength	$1.30 \times 10^6$	$V/m$
$h$	Channel height	$1.00 \times 10^{-3}$	$m$
$n$	Particle number density	$3.73 \times 10^{11}$	$1/m^3$
$\varepsilon_1$	Permittivity of carrier liquid	$3.27 \times 10^{-11}$	$C^2/Nm^2$
$\varepsilon_2$	Permittivity of particles	$2.30 \times 10^{-11}$	$C^2/Nm^2$
$\phi$	Solid volume fraction of the particles	$1.00 \times 10^{-1}$	----
$\eta_0$	Carrier liquid viscosity (no particles)	$1.20 \times 10^{-2}$	$Pa \cdot s$
$\eta'$	Spin viscosity	0	$N \cdot s$
$\eta$	Zero field fluid viscosity (w/ particles)	$1.53 \times 10^{-2}$	$Pa \cdot s$
$\eta_e$	$\eta_e = \eta + \zeta$	$1.76 \times 10^{-2}$	$Pa \cdot s$
$\sigma_1$	Conductivity of the carrier liquid	$4.00 \times 10^{-8}$	$S/m$
$\sigma_2$	Conductivity of the particles	$1.00 \times 10^{-14}$	$S/m$
$\tau_{MW}$	Maxwell-Wagner relaxation time	$1.11 \times 10^{-3}$	$s$
$\zeta$	Vortex viscosity	$1.80 \times 10^{-3}$	$Pa \cdot s$

Figure  
[Click here to download high resolution image](#)

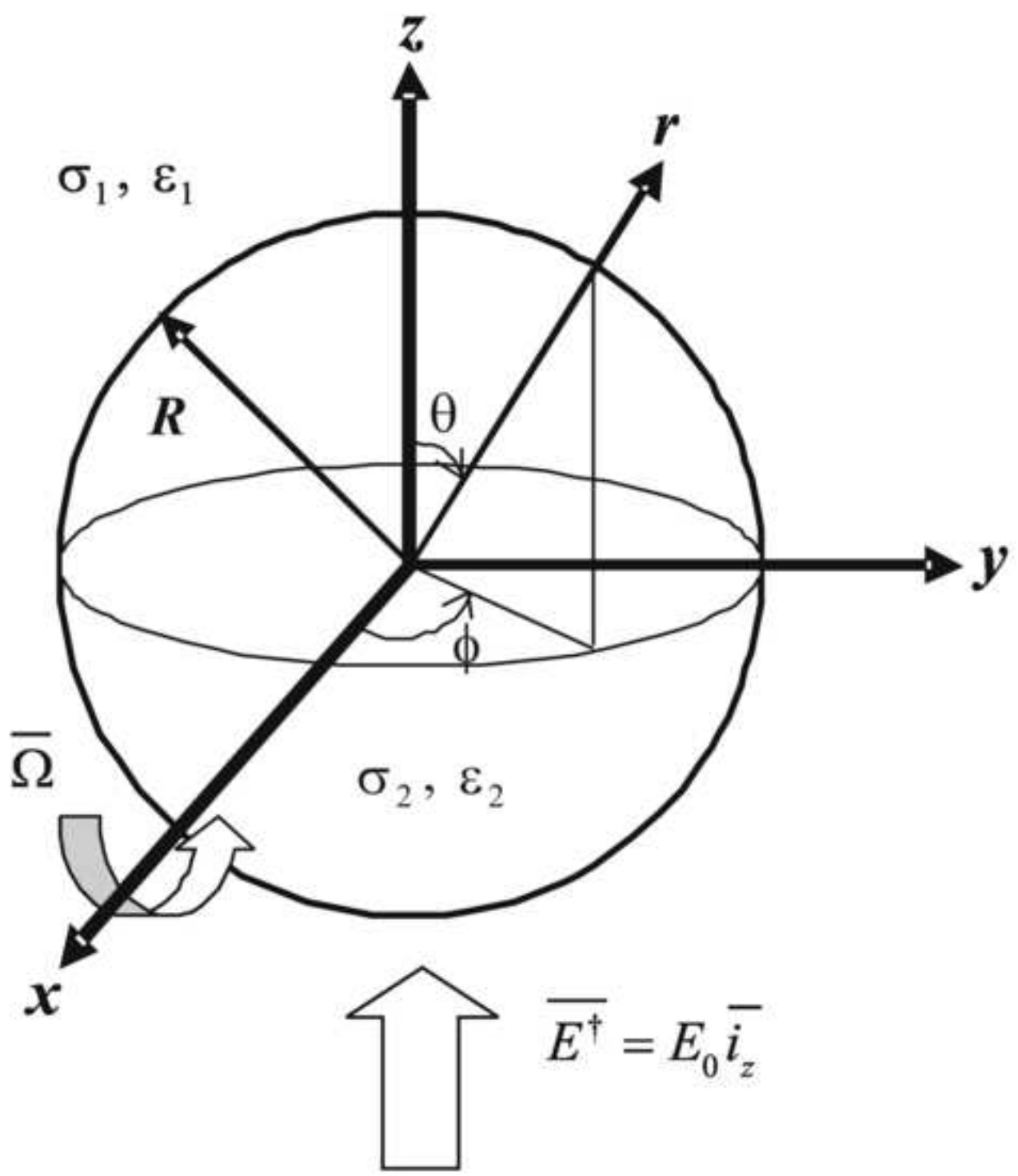


Figure  
[Click here to download high resolution image](#)

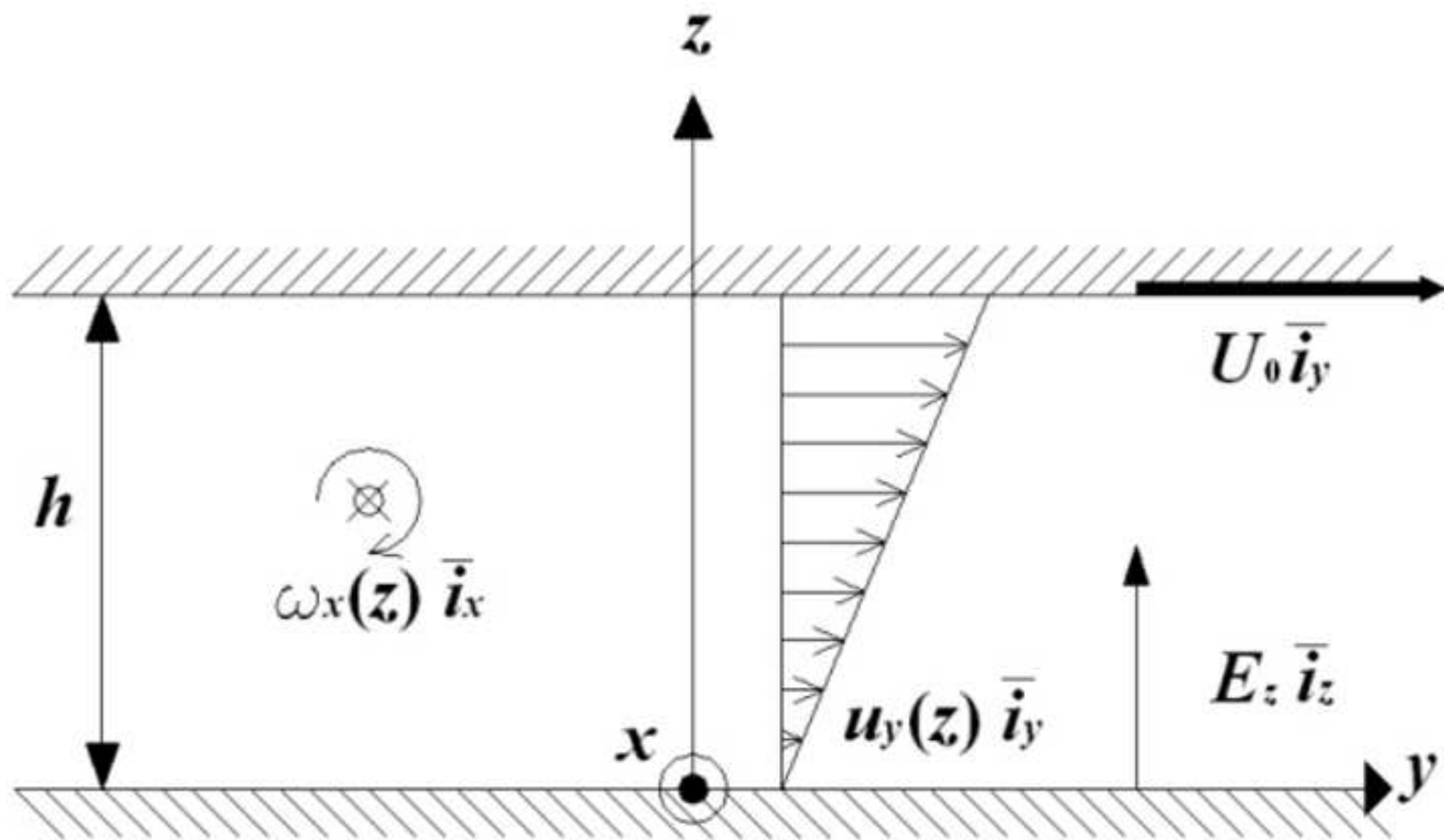


Figure  
[Click here to download high resolution image](#)

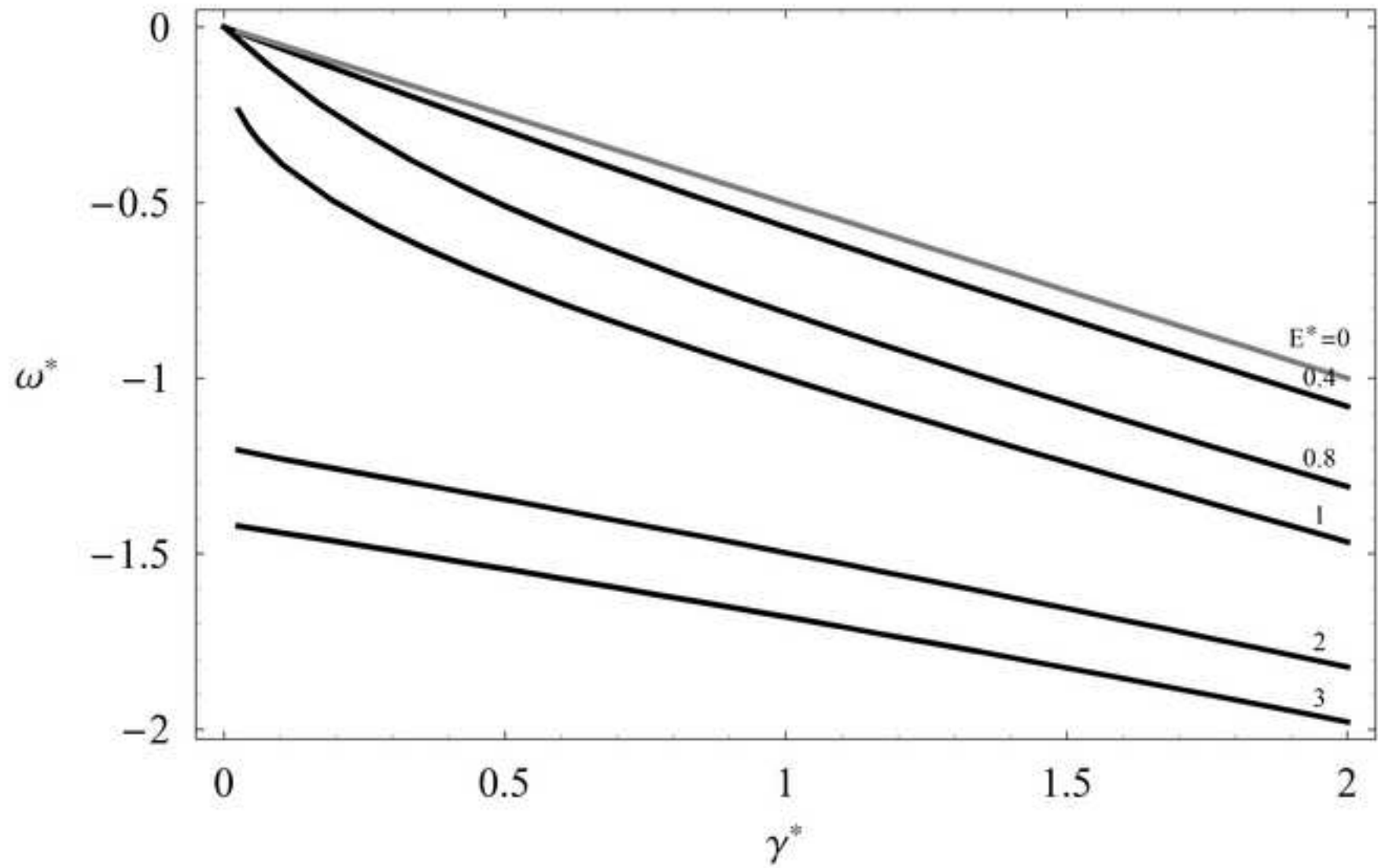


Figure  
[Click here to download high resolution image](#)

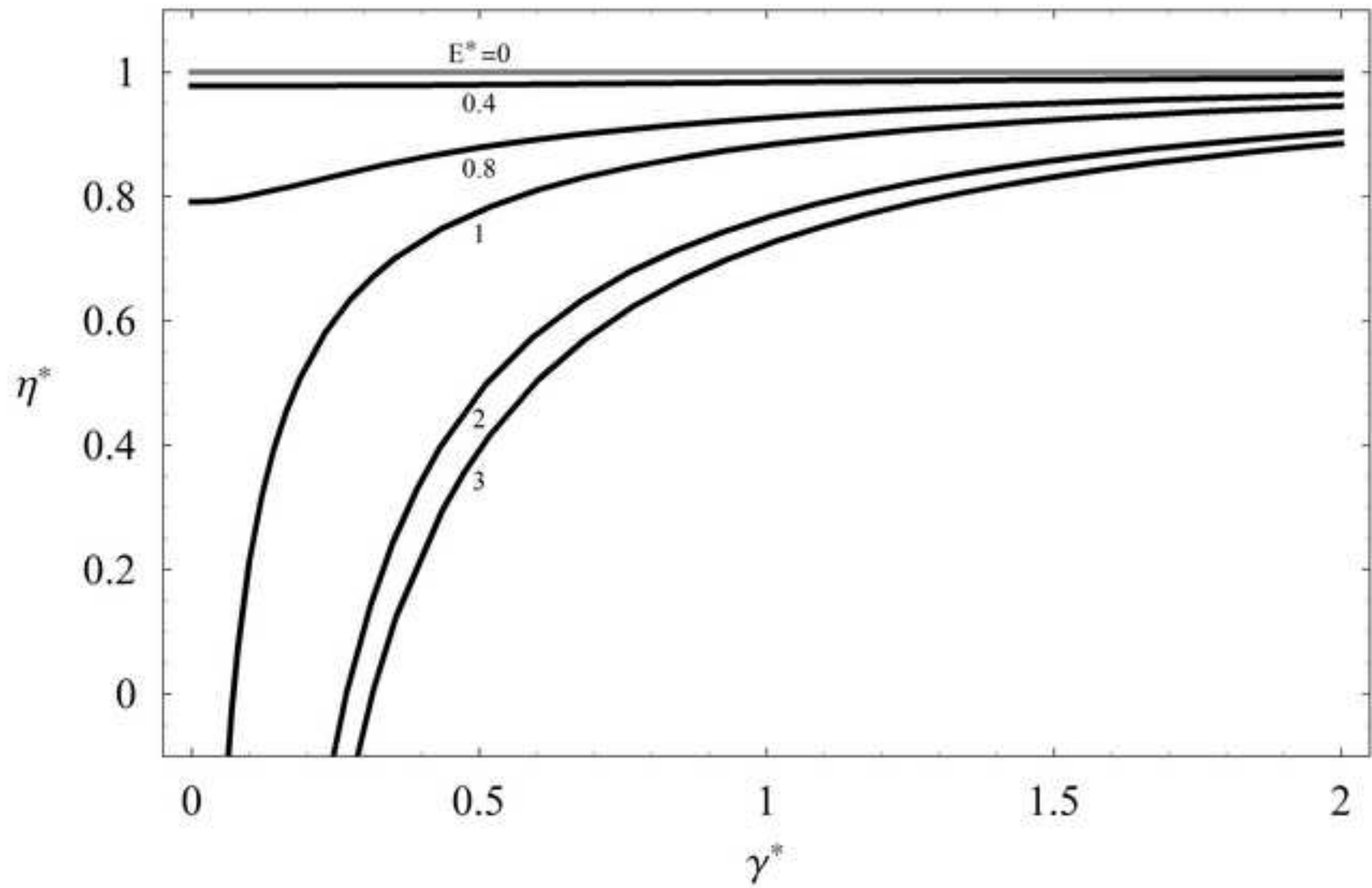


Figure  
[Click here to download high resolution image](#)

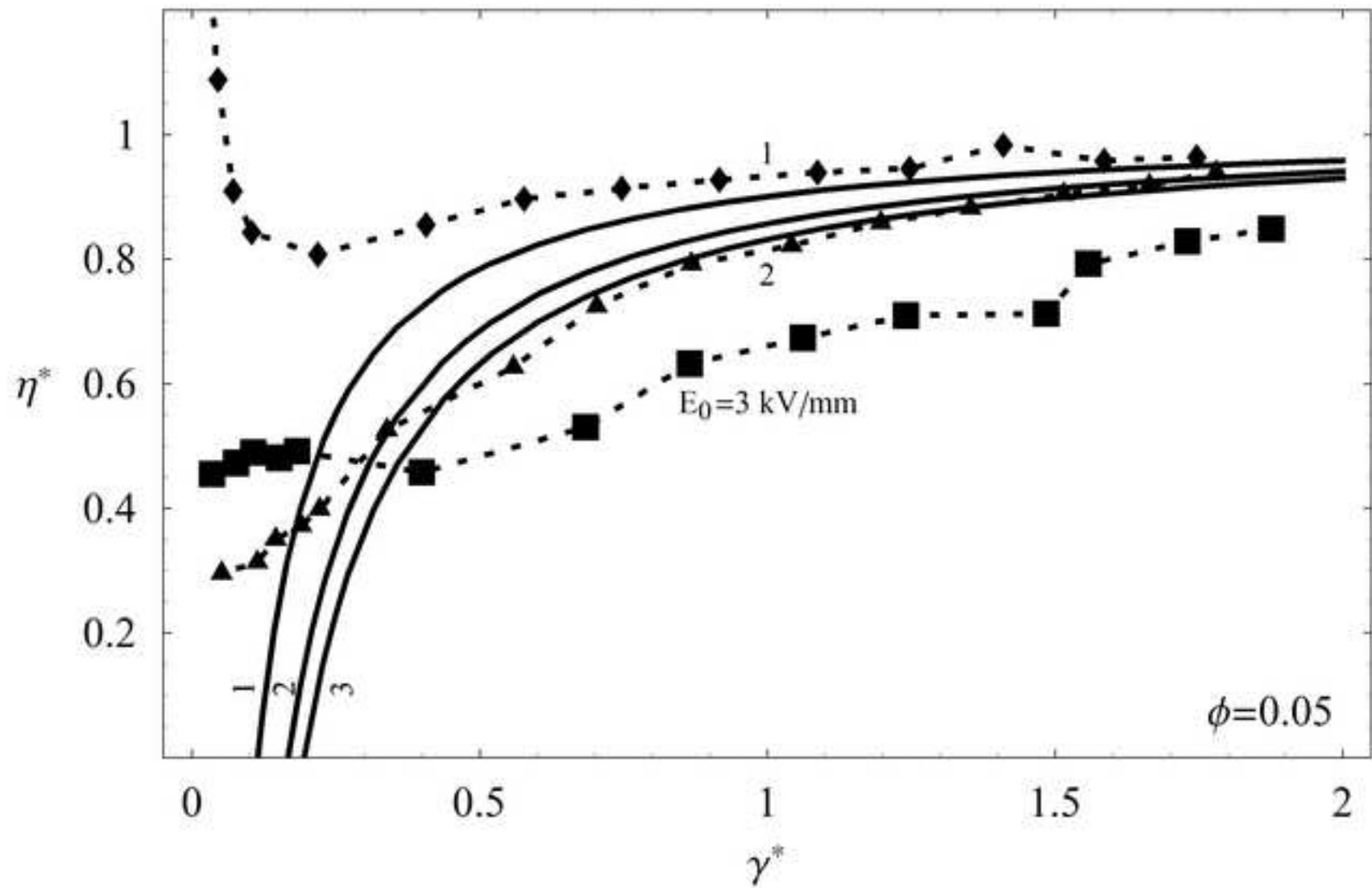


Figure  
[Click here to download high resolution image](#)

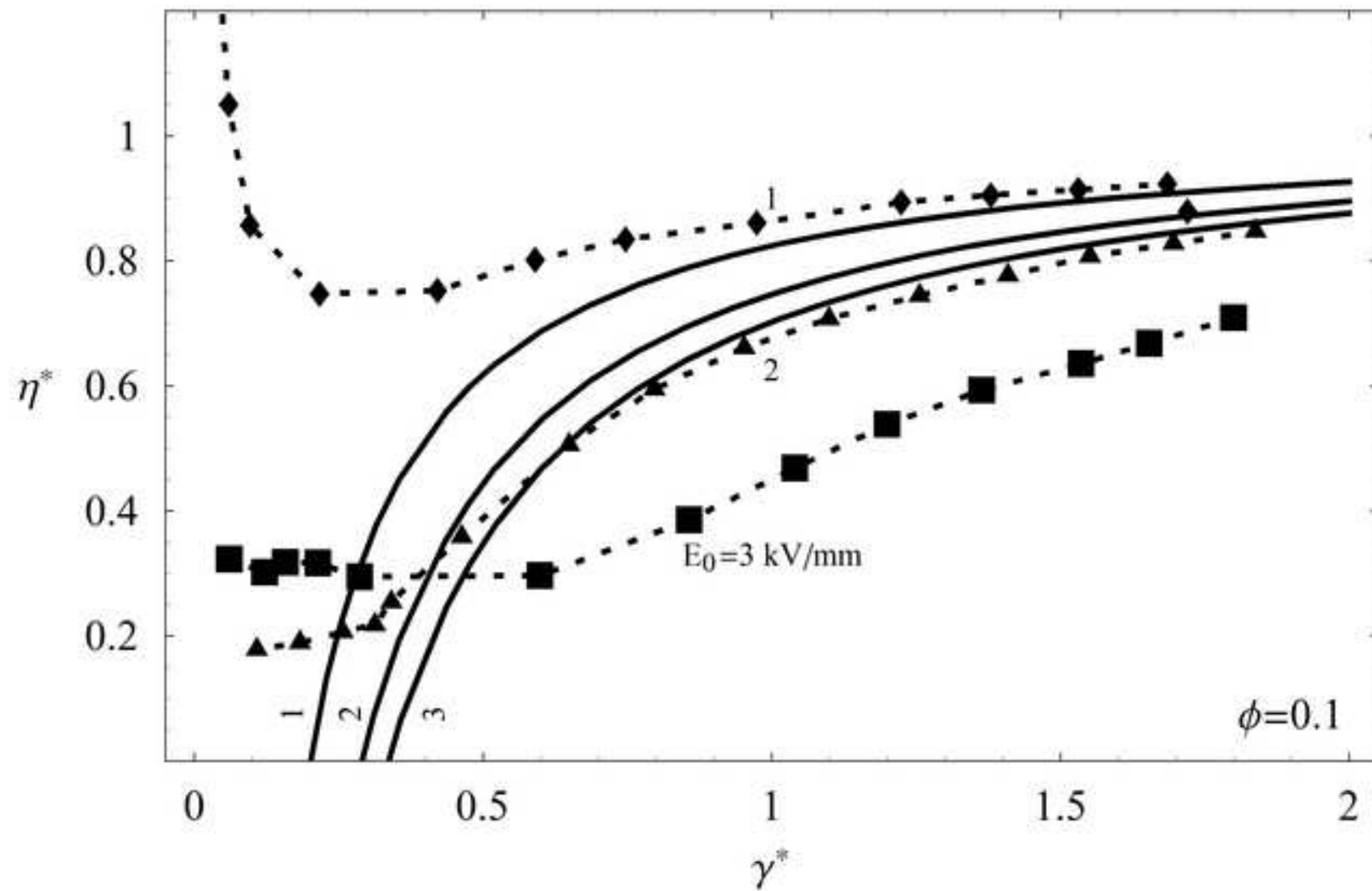




Figure  
[Click here to download high resolution image](#)

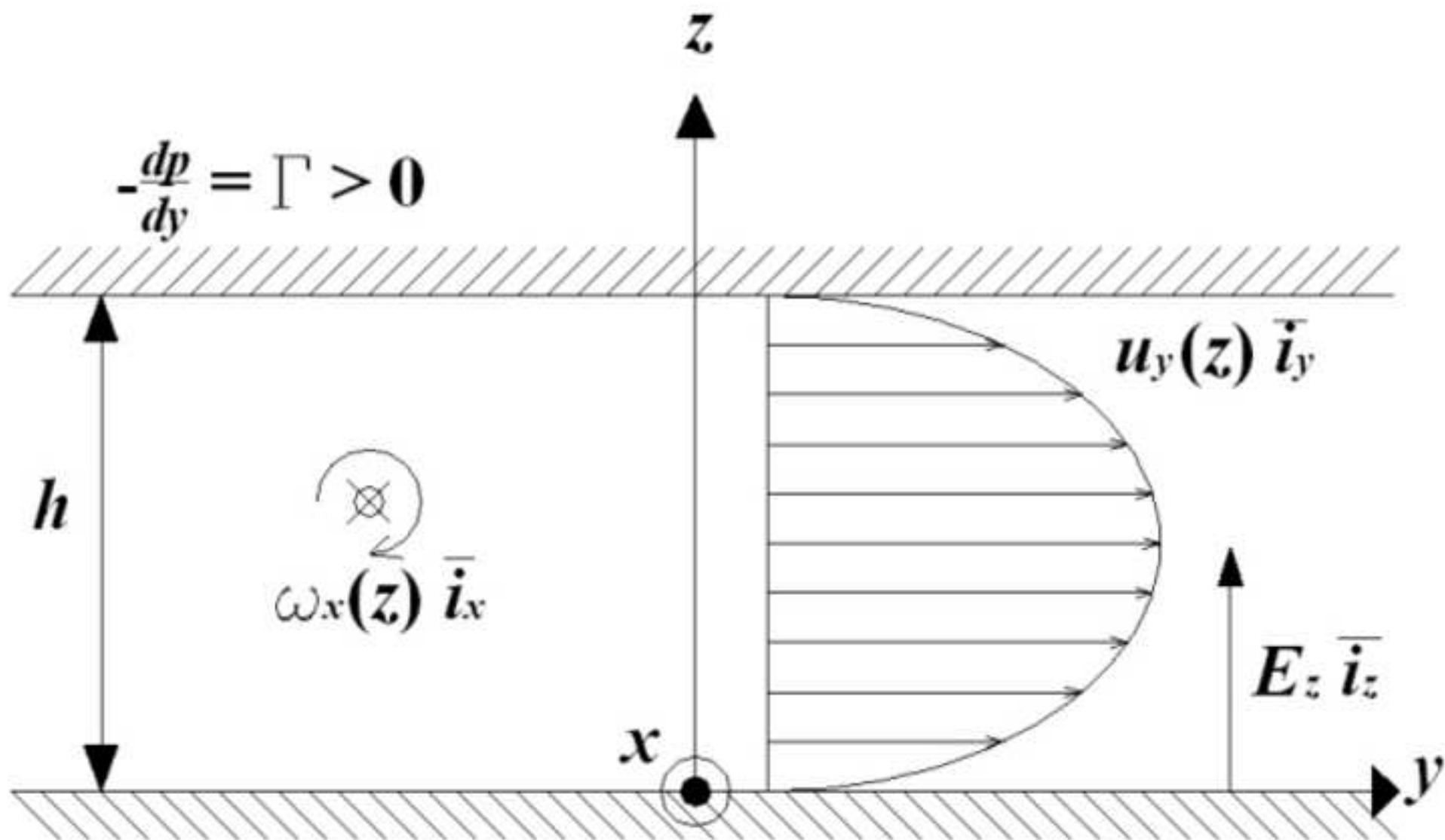


Figure  
[Click here to download high resolution image](#)

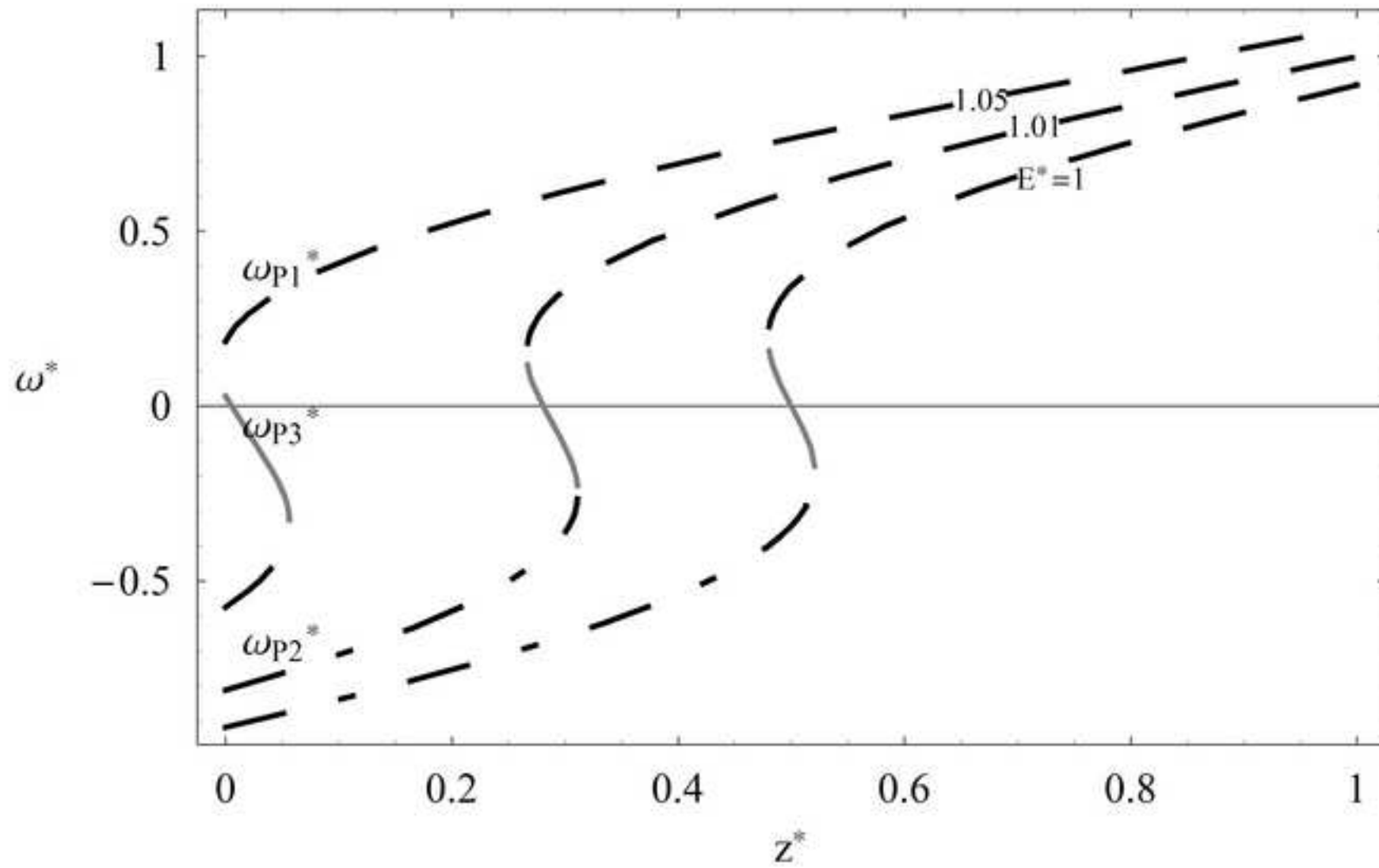


Figure  
[Click here to download high resolution image](#)

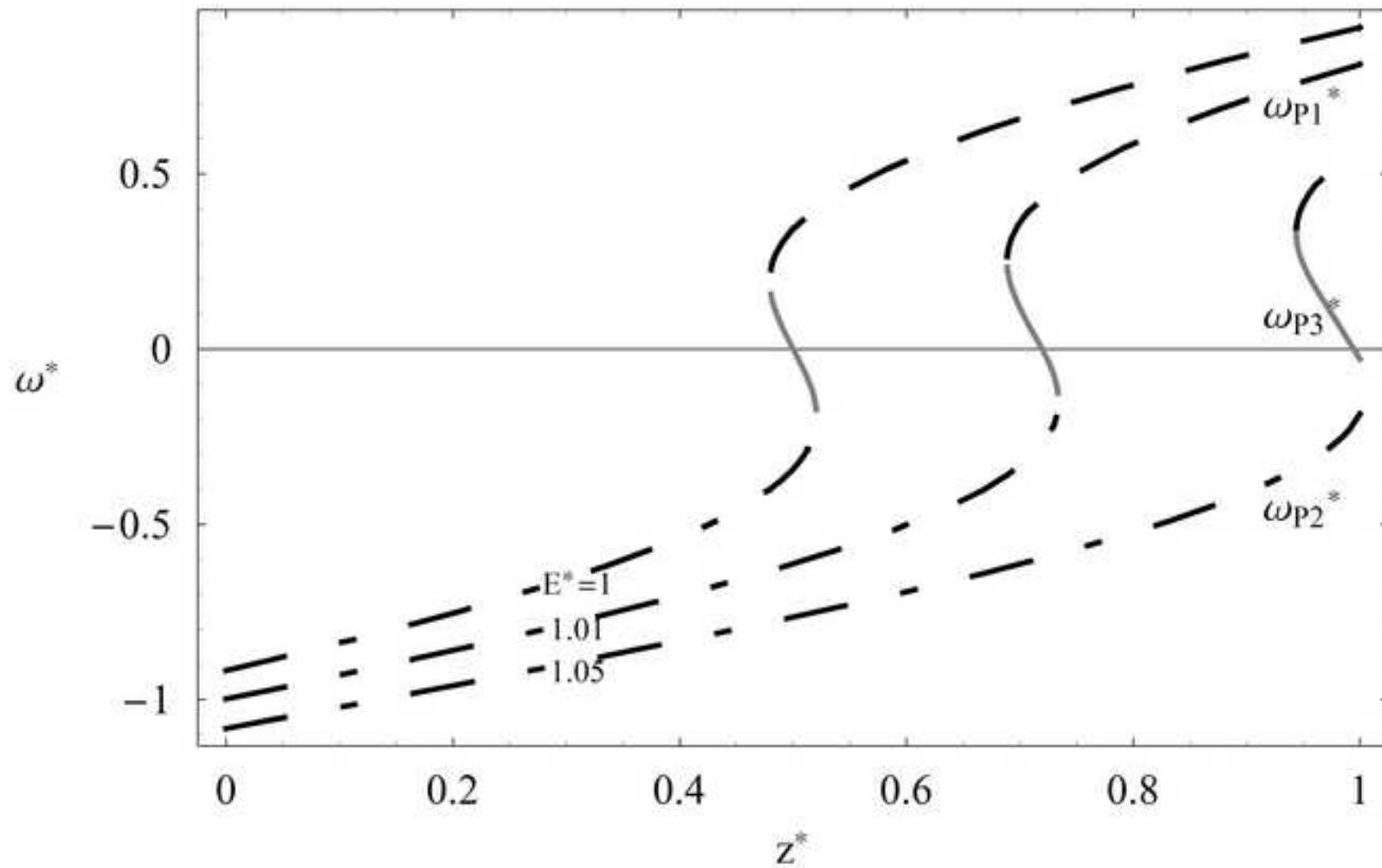
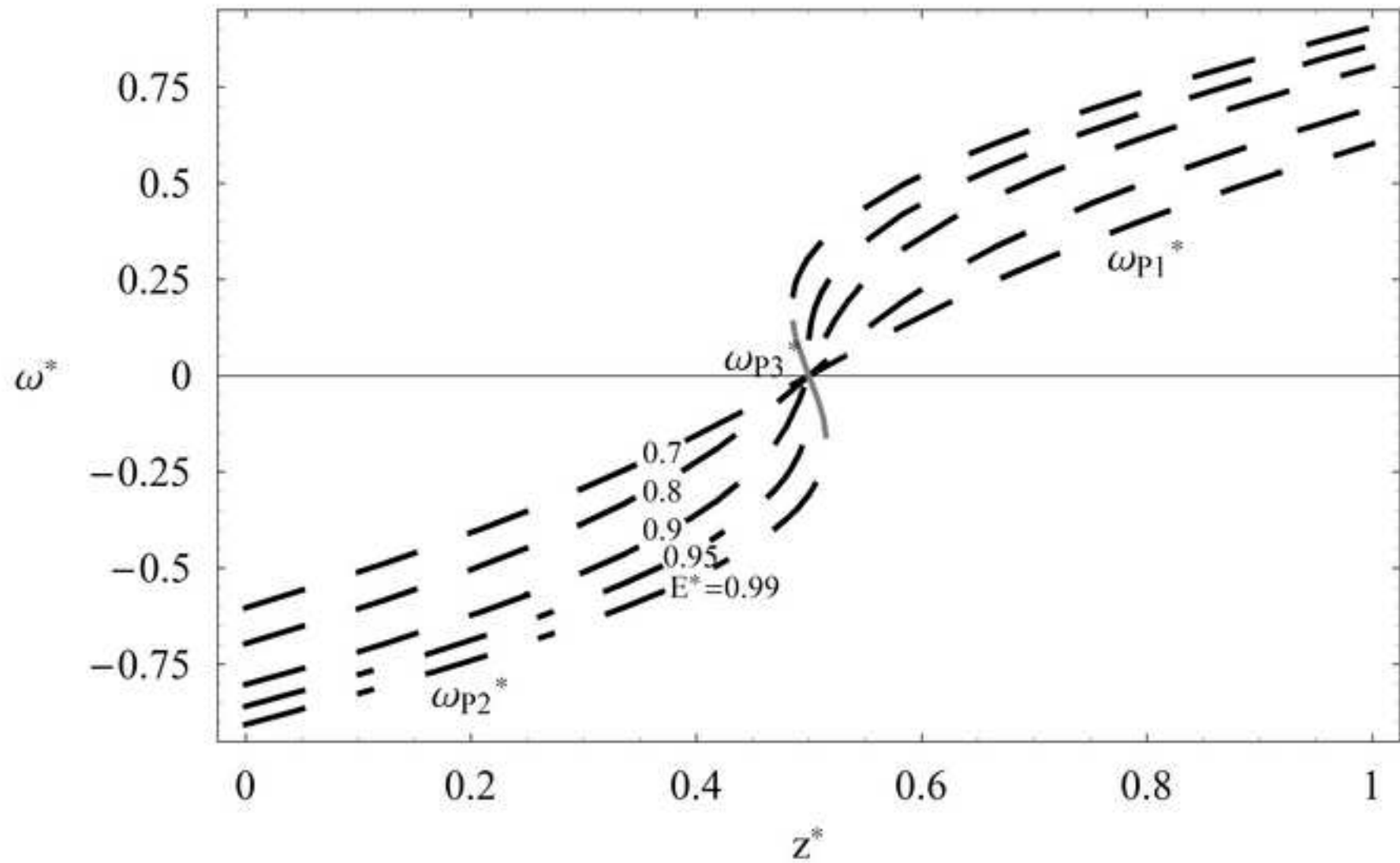
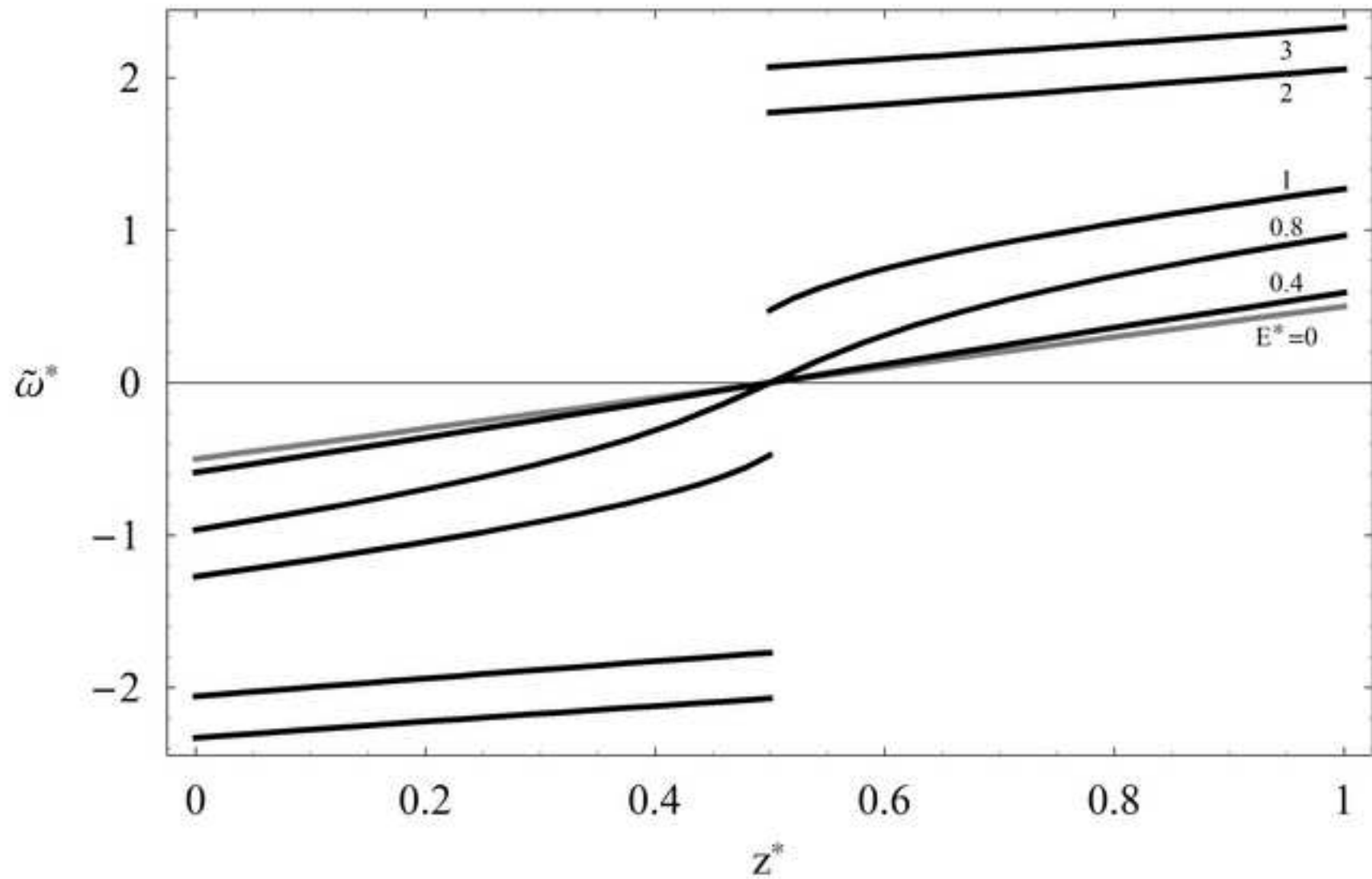


Figure  
[Click here to download high resolution image](#)



Figure

[Click here to download high resolution image](#)



Figure

[Click here to download high resolution image](#)

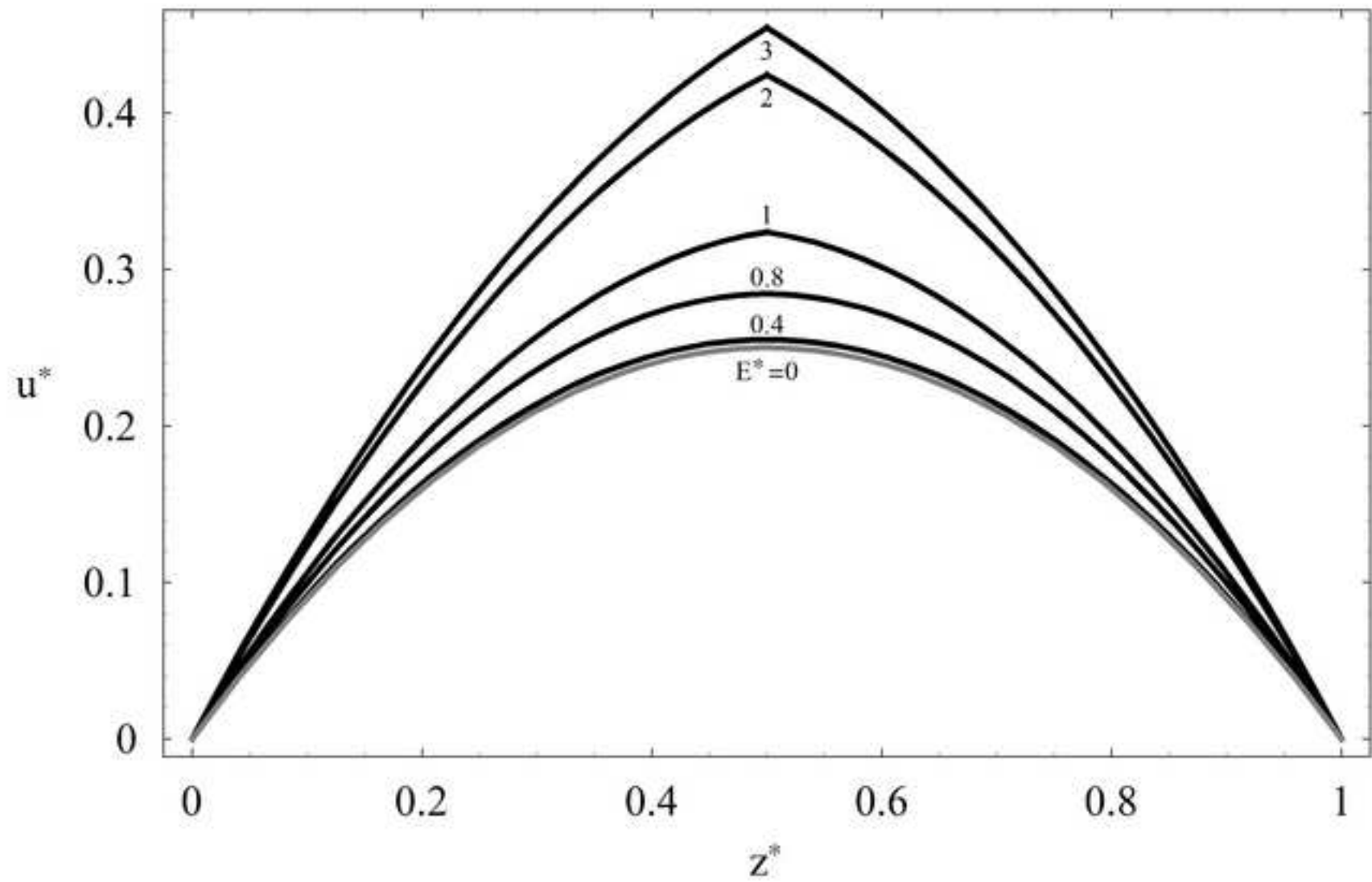


Figure  
[Click here to download high resolution image](#)

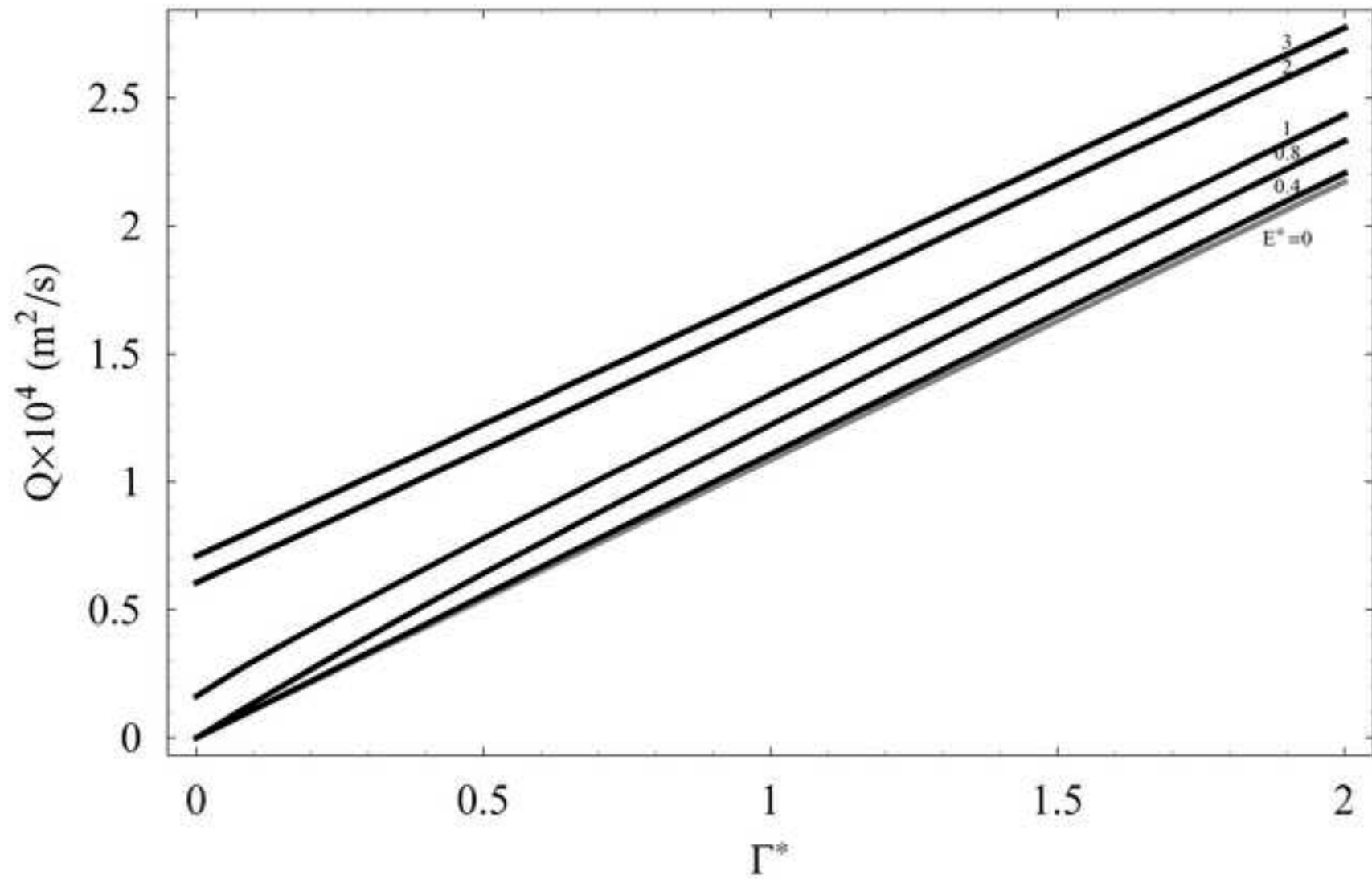


Figure  
[Click here to download high resolution image](#)

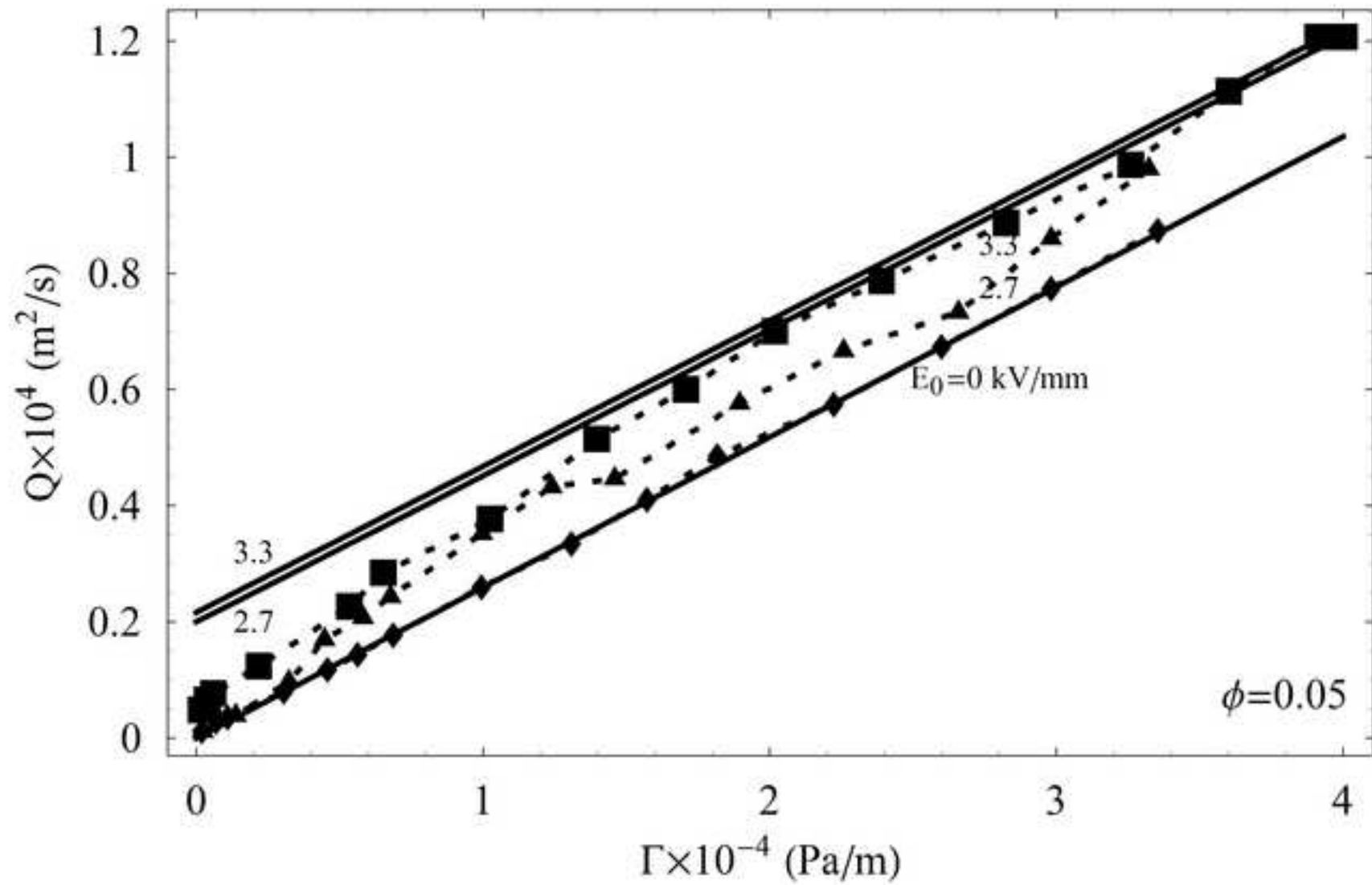




Figure  
[Click here to download high resolution image](#)

